Properties of the Yellow Sea Meteotsunamis in Spring

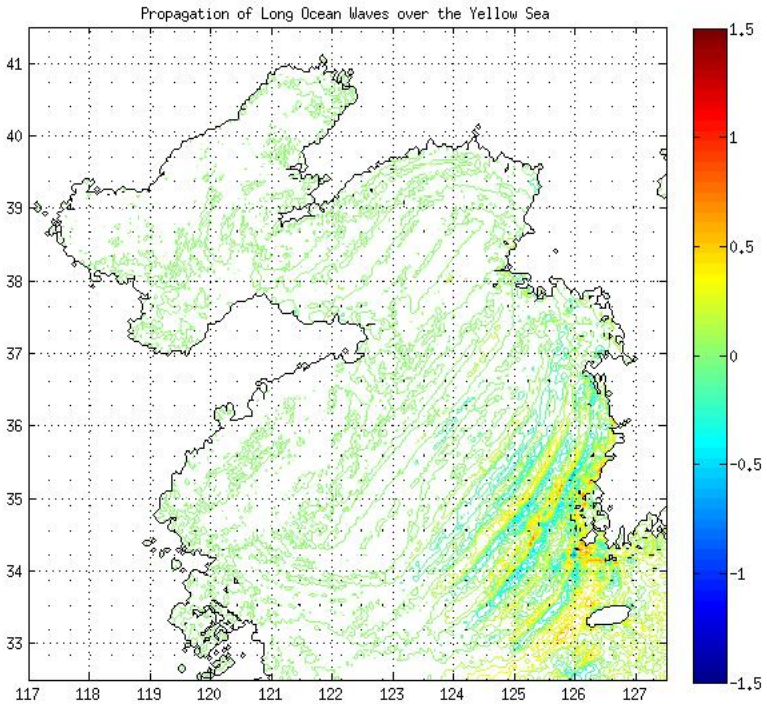

Master Thesis on Meteorology

Yong-Seong Kang

University of Bergen
Geophysical Institute

Cover illustration:
Simulated long ocean waves induced by an atmospheric disturbance in the Yellow Sea. The west coast of South Korea experiences in average a couple of meteotsunami events every year. Most of them occur in spring when an atmospheric disturbance approaches the area at a speed of about 26 m/s close to that of barotropic surface waves.

Contents

List of Figures

List of Tables

Abstract

This paper documents the properties of the Yellow Sea meteotsunamis in spring based on a total number of 49 meteotsunami events in spring (Mar-May) between 2002 and 2013 documented by the Korea Meteorological Administration (KMA).

The typical synoptic setting for the meteotsunami events is that an intense positive relative vorticity max forms over Manchuria, which is triggered by the development of the jet stream from the north-west. The relative vorticity max generates atmospheric disturbances over the Yellow Sea, which move at a favourable speed, about 26 m/s, for the Proudman resonance. There are two different patterns in atmospheric disturbance movement, approaching from the north-west and the south-west, which are associated with the evolving atmosphere to the most favourable synoptic setting for a meteotsunami in the Yellow Sea. In general, the SW pattern occurs during times in transit to and from the typical setting, whereas the NW pattern takes place more likely at the mature typical setting. During the evolution of the typical synoptic setting, the vorticity max generates disturbances consecutively for a couple of days, which is attributed to the high frequency of occurrence of meteotsunami in the Yellow Sea in spring.

Mean properties of the Yellow Sea meteotsunamis in spring can be expressed as: a mean atmospheric disturbance, with a pressure change of 3.2 hPa for 37 min, generates tsunami-like sea level oscillations at the west coast with a mean sea level of 21.5 cm by an amplification factor of 6.3 due to the Proudman resonance, shelf effect and harbour resonance.

According to the numerical simulation, the disastrous event on 31 March 2007 at the west coast is due to high-frequency waves of 20-30 m with periods of 2-8 min at the entrance of harbours/bays/inlets, which were amplified due to the Proudman resonance and shelf effect. The incoming waves are considered to have been further heightened up to about 130 cm due to harbour resonance. The energy source of those record-high waves is an intense disturbance with a pressure jump of 2 hPa for 4 min, characterised by a high energy transfer efficiency from the disturbance to long ocean waves.

A Introduction

Travelling air pressure disturbances generate long waves in the open ocean and amplify them into tsunami-like waves near the coast through specific resonance mechanisms. Such tsunami-like waves have occasionally hit coasts in worldwide locations such as the Balearic Islands, Spain, the Black Sea, the western coast of Japan, Florida, U.S (Šepić et al., 2012). South Korea is no exception. Life losses and property damages by such disastrous waves have been reported three times during 2007-2011 at the west coast of South Korea (KMA, 2013).

Table 1: Damages caused by tsunami-like waves in the Yellow Sea in South Korea. These disasters are related with Events 15, 19 and 39 respectively in this study.

Occurrence	Place	Damage
31-Mar-2007	Yeonggwang	4 sea farms ruined 55 ships overturned Some residence area flooded
4-May-2008	Gunsan, Eocheongdo and Boryeong	9 people dead 15 people injured Several ships overturned
26-Apr-2011	Daeheuksando	Sea farms of 40 sectors ruined 4 ships sunk

Studies show that a sudden air pressure change, pressure jump, has a close relation with generation of long sea waves, which could lead to a meteorological tsunami: The meteorological mechanism responsible for an extraordinary *rissaga* event (the local name of high-amplitude sea level oscillations) with amplitude of 4-5 m occurred on 15 June 2006 at Ciutadella (Menorca, Spain) was an unusual pressure jump, associated with a convective squall line (Jansa et al., 2007). The air pressure disturbance, which propagated at a speed of about 21–24 m/s over the northern Adriatic shelf, generated open ocean waves through the Proudman resonance to cause the 1st meteotsunami in Adriatic Sea in 2007 (Šepić et al., 2009). The sea level oscillations of 16 events of tsunami-like sea level oscillations in the northern Adriatic between 1955 and 2010 are found to be coincident with pronounced atmospheric pressure disturbances characterized by a 2–4 hPa air pressure change over 10 min (Šepić et al., 2012).

Studies in South Korea also show that the Yellow Sea meteotsunamis also occur under such atmospheric disturbances: (i) the analysis of observation data reveals that sea level oscillations for 29-30 March 2007 coincided with atmospheric pressure disturbances moving eastward over the Yellow Sea (Cho et al., 2013), (ii) almost all the tsunami-like sea level oscillations are associated with pressure jumps over than 3 hPa for 1 h (KMA, 2013). Based on those findings, the Korea Meteorological Administration (KMA) has recently started to build up meteotsunami warning service infrastructure. However there is no enough understanding under which synoptic setting meteotsunami preferably occurs at the west coast of South Korea. Studies on this may need to take precedence in order to provide operational metheotsunami warning and forecasting service by forecasters. Thus this study focuses on synoptic analysis among other topics.

Šepić et al. (2012) describe the generation mechanism of tsunami-like waves as follows: (i) a pronounced air pressure disturbance, characterized by an abrupt air pressure change, is generated in the atmosphere; (ii) the air pressure disturbance transverses the open sea and resonantly transfers its energy to long-period sea waves; (iii) long-period sea waves reach bays where they may induce destructive seiches with wave heights of more than 3 m, and associated currents of several meters per second. Overall, an initial atmospheric pressure disturbance of as little as 3 hPa pressure change can result in a 300 cm high wave. When compared to the inverse barometric effect where 1 hPa of air pressure change corresponds to 1 cm of sea level change, this is multiplication of about 100 times. While the first step of generation mechanism is atmospherically conditioned, the second and third steps are strongly dependent on topographic properties, former more on the sea bathymetry and latter more on the characteristics of a coastline.

Regarding the first mechanism, this study aims at finding characteristics of synoptic setting under which atmospheric disturbances, leading to meteotsunamis, are favourable to occur over the Yellow Sea. Šepić et al. (2009) analysed 16 events of meteotsunami in the northern Adriatic between 1955 and 2010, and identified that typical conditions, under which pronounced air pressure disturbances occur, include a surface pressure low centred over the northern Adriatic, a temperature front at a height of approximately 850 hPa, and a strong south-westerly jet stream with wind speeds reaching 20–30 m/s at a height of approximately 500 hPa over the northern Adriatic. A total number of 92 meteotsunami events at the west coast of South Korea were documented, among which 49 occurred in spring (March-May) between 2002 and 2013 (Figure 1). We conducted analyses on the average atmospheric states and their main patterns during the 49 events (Section D.1).

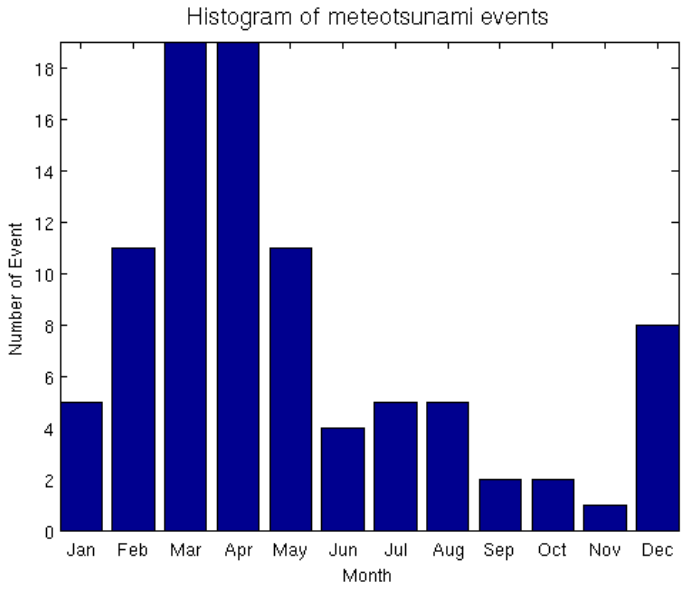

Figure 1: Distribution of occurrence time of meteotsunami events at the west coast of South Korea for 2002-2013 (after KMA (2013)).

The most common way of energy transfer between an air pressure disturbance and open sea waves is the Proudman resonance (Proudman, 1929). The Proudman resonance occurs when an air pressure disturbance transverses the sea of uniform of slowly changing depth. For the Proudman resonance to occur, an air pressure disturbance should propagate with a speed U which is equal to or close to a speed of barotropic sea waves c. As for the third step of generation mechanism, it occurs when atmospherically generated open sea waves hit bays which are prone to strong seiche activity, i.e., which have large top-to-mouth amplification factor (Rabinovich, 2009). Such bays are usually rather elongated and narrow and very shallow at the closed end (Monserrat et al., 2006). If incoming sea waves have a significant energy at a seiche period of such a bay, seiches in the bay can be enhanced to destructive heights.

Only 10 tide gauges among 22 along the west coast detected tsunami-like sea level oscillations (Figure 17) between 2002 and 2013. This suggests that geographical locations affect occurrence of meteotsunamis. Regarding the above second and third mechanisms, we conducted wavelet analysis to identify resonance properties at the 10 sites. In addition, we performed wavelet analysis on mean sea level pressure (MSLP) time series during the events from the sites on the west coast to analyse dominant frequencies of atmospheric disturbances (Section D.2).

Finally, we conducted two numerical experiments to simulate propagations of long ocean waves for an event mean and for the event on 31 March 2007 (Event 15) in Section D.3.

In Section B, theories employed for the study, in Section E discussion on linkages between the sections, and in Section F summary of the paper are given.

B Theory

Atmospheric pressure is a source affecting sea level. In a normal case, atmospheric pressure changes can generate small-scale sea level oscillation with periods of a few minutes to a few hours. When a cyclone passes over a large ocean region, sea level increases due to the inverted barometer effect, while an anticyclone lowers sea level. It is known that a change of 1 hPa corresponds to a sea level change of 1 cm. Atmospheric fluctuations however can produce a significant sea level response when some form of resonance occurs between the ocean and the atmospheric forcing. During resonance, the atmospheric disturbance

propagating over the ocean surface is able to generate significant long ocean waves by continuously pumping energy into these waves (Monserrat et al., 2006). Those resonances includes: (i) "Proudman resonance" (Proudman, 1929), when the atmospheric disturbance moves over an ocean at the longwave phase speed, (ii) "shelf resonance", when the atmospheric disturbance and associated atmospherically generated ocean wave have periods and/or wavelength equal to the resonant period and or wavelength of the shelf region and (iii) "harbour resonance", when a harbour is reached by ocean waves with the same frequency with the natural resonance frequency of the harbour.

B.1 Proudman resonance

Proudman (1929) showed the effects of atmospheric pressure on the change of sea level by considering ideal basins and problems of three types: (i) a narrow channel with the depth to be uniform and the currents to be entirely in one direction, (ii) a channel whose depth varies from side to side, but over which the conditions are uniform along its length, and (iii) a sea of uniform depth and of unbounded lateral extent in all directions, and the conditions to be symmetrical about a point.

The 1D shallow water equations may be written as:

$$\frac{\partial u}{\partial t} = -g\frac{\partial}{\partial x}(\zeta - \bar{\zeta}), \tag{1}$$

$$\frac{\partial \zeta}{\partial t} + \frac{\partial}{\partial x}(hu) = 0 \tag{2}$$

where g is the acceleration of gravity, h is the depth of the sea at any point, t is the time, x is x component of Cartesian coordinates in the plane of the undisturbed surface of the sea, u is the component of the current in the direction of the x-Cartesian axis, at any point and time, ζ is the elevation of the free surface of the sea above its mean level at any point and time, and $\bar{\zeta}$ is the variable part in the height of the "sea-water barometer" at any point and time.

The Proudman's equilibrium-solution of ζ for a channel of constant depth unbounded to both directions under the initial condition, $\zeta = 0$ and $u = 0$, is expressed as:

$$\zeta = \frac{1}{1-(U/c)^2}F(x-Ut) - \frac{1}{2}\frac{1}{1-U/c}F(x-ct) - \frac{1}{2}\frac{1}{1+U/c}F(x+ct) \tag{3}$$

where U is a constant speed of atmospheric disturbance and $F()$ denotes any functions of their arguments, c is the phase speed of the waves and $\bar{\zeta} = F(x-Ut)$.

From this, the atmospherically induced forced wave in the open ocean may be described by the well-known "Proudman expression":

$$\Delta\zeta \approx \frac{\Delta\bar{\zeta}}{1-Fr^2} \tag{4}$$

where $Fr = U/c$ is the Froude number, and $\Delta\bar{\zeta} = -\Delta P_a/\rho g$ is sea level change due to the inverse barometric effect, where ΔP_a is the atmospheric pressure disturbance and ρ is the water density. Equation 4 says that the contribution to the sea level change by atmospheric disturbance, $\Delta\zeta/\Delta\bar{\zeta}$, is maximized when the atmospheric disturbance translational speed U equals the ocean wave phase speed $c = \sqrt{gh}$ in an unbounded ocean.

B.2 Shelf resonance

A shelf resonance occurs when long waves excites one of the resonant modes of a region. The effect is most striking when a shelf is about a quarter wavelength wide of the longwave.

B.3 Harbour resonance

Harbour oscillations (coastal seiches) are a specific type of seiche motion that occur in partially enclosed basins (bays, fjords, inlets, and harbours) that are connected through one or more openings to the sea. Harbour oscillations are mainly generated by long waves entering through the open boundary (harbour entrance) from the open sea. Important property of harbour oscillations include the Helmholtz mode (pumping mode) of a harbour, the frequency of the incoming waves and the "Q-factor" (Monserrat et al., 2006).

The amplification factor for long waves impinging on a harbour from the open sea is:

$$H^2(f) = \frac{1}{(1 - f/f_0)^2 + Q^{-2}(f/f_0)^2} \tag{5}$$

where f is the frequency of the long waves, f_0 is the resonant frequency of the harbour, and Q is the quality factor (Q-factor), which is a linear measure of the energy damping in the system defined as follows:

$$Q^{-1} = \frac{dE/dt}{\omega E} = -2\beta \tag{6}$$

where $E = E_0 e^{-2\beta\omega t}$ is the energy of the system as it decays from an initial value E_0, β is a dimensionless damping coefficient, and $\omega = 2\pi f$ is the angular frequency. At resonance, $f = f_0$, and the power amplification factor attains the value Q^2. The factor decreases to unity for $f = 0$ and goes to zero as f goes to infinity. Therefore, Q for harbour oscillations plays a double role: it is a measure of the resonant increase of wave heights for the waves arriving from the open ocean and also acts as an index of the time decay rate of wave heights inside the harbour. Narrowing the harbour entrance increases the quality factor Q and, consequently, the amplification of the arriving waves. That is why significant seiches are normally observed only in elongated and narrow inlets (fjords) or for bays (harbours) with narrow entrances.

As indicated by expression equation 5, a large Q-factor is crucial but that intense harbour oscillations can be produced only for the resonant case of matching between the dominant frequency (f) of the arriving (external) waves and an eigenfrequency f_0 of the harbour (normally, the eigenfrequncy of the fundamental or Helmholtz harbour mode). This means that catastrophic harbour oscillations are the result of a "double resonance effect": (i) "external resonance" between the moving atmospheric disturbance and the open-ocean waves; and (ii) "internal resonance" between the arriving open-ocean waves and the fundamental eigenmode of the harbour (bay, inlet) (Rabinovich, 2009).

B.4 Isochronal methods for estimation of movements of waves

To estimate velocities of long-period ocean waves and atmospheric waves, isochronal analysis method is useful, which is based on the assumption that the waves propagate as plane waves with uniform speed and direction (e.g. Eom et al. (2012), Thomson et al. (2009) and Vilibić et al. (2008)). In this case, the theoretical arrival time is a linear function of position.

Meteotsunami Propagation Algorithm (MPA)

Eom et al. (2012) used the Meteotsunami Propagation Algorithm (MPA) to estimate propagation of meteotsunami. This method, which assumes that the wave crest is straight and propagates to the direction perpendicular to the crest until the next known destination (Figure 2). Assuming t_1 and t_2 are the arrival times of the meteotsunami at tide sites P_1 and P_2 respectively, the time lag is expressed as: $dt_{21} = t_2 - t_1$. Let us assume that the crest is straight when the waves are passing P_1. First, using depth data at P_2, the speed of propagating waves at P_2 may be estimated by the phase speed of the wave: $c_2 = \sqrt{gh_2}$. Second, the propagated distance between P_1 and P_2 may be estimated as: $R_{21} = c_2 \times dt_{21}$. Third, we may find a tangent line, passing the first site (P_1), to a circle (O_2) with the propagated distance (R_{21}) as its radius at a point (a_2, b_2) by:

$$(a_2 - x_2)(x - x_2) + (b_2 - y_2)(y - y_2) = R_{21}^2 \tag{7}$$

This line passes P_1, so:

$$(a_2 - x_2)(x_1 - x_2) + (b_2 - y_2)(y_1 - y_2) = R_{21}^2 \tag{8}$$

In addition the tangent, (a_2, b_2), is on O_2, so:

$$(a_2 - x_2)^2 + (b_2 - y_2)^2 = R_{21}^2 \tag{9}$$

We may find the tangent point, (a_2, b_2), from equations 8 and 9, and then the tangent line, W_1 from equation 7. Finally we may find the estimated direction d_1 from the tangent line. Likewise we may estimate the following directions from the data from next stations.

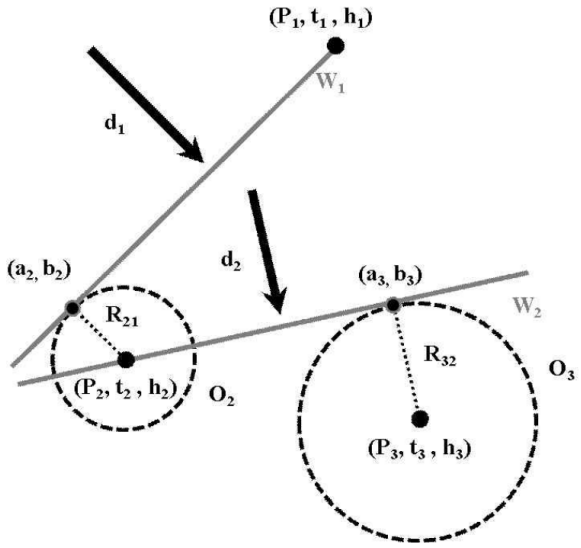

Figure 2: Illustration of MPA (Eom et al., 2012)

Pressure Gradient Method (PGM)

Vilibić et al. (2008) used the Pressure Gradient Method (PGM) to estimate the speed and direction of travelling atmospheric disturbance based on observations on a triangle of pressure stations with coordinate: $(x_1 = 0, y_1 = 0)$, (x_2, u_2) and (x_3, y_3) (Figure 3). Assuming the waves do not change during its travel

over the domain and have a constant speed and direction, a simple plane geometry yields the following expressions:

$$\tan\phi = a = \frac{t_3 y_2 - t_2 y_3}{t_3 x_2 - t_2 x_3} \tag{10}$$

$$U = \frac{1}{t_2}\frac{y_2 - a x_2}{\sqrt{1+a^2}} = \frac{1}{t_3}\frac{y_3 - a x_3}{\sqrt{1+a^2}} \tag{11}$$

where $(x_1 = 0, y_1 = 0)$, (x_2, y_2) and (x_2, y_2) are the positions of the pressure stations, t_2 and t_3 are time lags between stations 2 and 3 and station 1, a is the slope of the axis tangential to the direction of the waves, and U is the speed of the movement of the waves. Here the time lags can be derived from the different arrival times of the atmospheric disturbance, which is described in the following section (e.g. KMA (2013)).

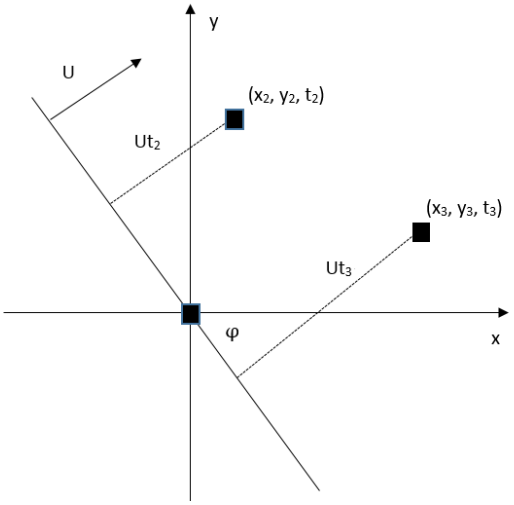

Figure 3: Illustration of the detection of the atmospheric disturbance speed (U) and direction (ϕ) by using data from a triangle of stations.

B.5 EOF Analysis

A useful technique for compressing the variability in a large time-series data is principal component analysis (PCA), or empirical orthogonal function (EOF) analysis. The advantage of EOF analysis is that it provides a compact description of the spatial and temporal variability of data series in terms of orthogonal functions, or statistical "modes." EOFs can be used in both the time and frequency domains (Emery and Thomson, 2004).

Assume a matrix F whose dimension is $n \times p$, where n represents time domain $(t_1, t_2, ...t_n)$ and p space domain $(x_1, x_2, ..., x_p)$, i.e., each row is one map, and each column is a time series of observations for a given location. Matrix F can be reconstructed as:

$$F = \sum_{j=1}^{p} \vec{a_j}(EOF_j) \tag{12}$$

where $\vec{a_j}$ are the principal component time series (PCs) or the expansion coefficients of the EOFs. Here EOFs are found from the eigenvalue problem:

$$RC = C\Lambda \tag{13}$$

where C is the covariance matrix of F, and Λ is a diagonal matrix containing the eigenvalues λ_i. For each eigenvalue λ_i, we find the corresponding eigenvector c_i. Each of these eigenvectors can be regarded as a map, the EOFs. Each eigenvalue λ_i, gives a measure of the fraction of the total variance in R explained by the mode. This fraction is found by dividing the λ_i by the sum of all the other eigenvalues (the trace of Λ).
The pattern, obtained when an EOF is plotted as a map, represents a standing oscillation. The PCs represent how the pattern oscillates in time. The "modes of variability" that the EOFs show are primarily data modes, and not necessarily physical modes. Whether they are physical will be a matter of subjective interpretation (Bjornsson and Venegas, 1997).

B.6 Wavelet analysis

Wavelet analysis is a commonly used technique for analysing localized variations of power within time series. It decomposes a time series into time-frequency (period) space, thus enabling determination of both how the dominant period modes of variability and locally averaged power vary in times (Torrence and Compo, 1998).
The continuous wavelet transform of a time series $x_n(n = 0, ..., N-1)$ is defined as the convolution of x_n with a scaled and translated version of a wavelet basis function, for example, Morlet wavelet function $\psi_0(\eta) = \pi^{-1/4} e^{i\omega_0\eta} e^{-\eta^2/2}$:

$$W_n(s) = \sum_{n'=0}^{N-1} x_{n'} \psi^* \frac{(n'-n)\delta t}{s} \tag{14}$$

Here * indicates the complex conjugate. By varying the wavelet scale s and translating along the localized time index n, one can construct a picture showing both the amplitude of any features versus the scale and how this amplitude varies with time.
Because the Morlet wavelet function $\psi(\eta)$ is complex, the wavelet transform $W_n(s)$ is also complex, so one can define the wavelet power spectrum as $|W_n(s)|^2$.
The Morlet wavelet with $\omega_0 = 6$ gives a value of $\lambda = 1.03s$, where λ is the Fourier period, indicating that for the Morlet wavelet the wavelet scale is almost equal to the Fourier period. Therefore, in this paper, we use both scale and period with the same meaning.

B.7 Meteotsunami model

Vilibić et al. (2008) used the following non-linear shallow water model to simulate the destructive meteotsunami of 15 June 2006 on the coast of the Balearic Islands. The model is based on the momentum equations containing the air pressure forcing term and the continuity equation:

$$\frac{\partial U}{\partial t} + \frac{U}{(h+\zeta)}\frac{\partial U}{\partial x} + \frac{V}{(h+\zeta)}\frac{\partial V}{\partial y} - fV = -g(h+\zeta)\frac{\partial \zeta}{\partial x} - \frac{gU(U^2+V^2)^{1/2}}{C^2(h+\zeta)^3} - \frac{h+\zeta}{\rho}\frac{\partial p}{\partial x} \tag{15}$$

$$\frac{\partial V}{\partial t} + \frac{U}{(h+\zeta)}\frac{\partial V}{\partial x} + \frac{V}{(h+\zeta)}\frac{\partial V}{\partial y} + fU = -g(h+\zeta)\frac{\partial \zeta}{\partial y} - \frac{gV(U^2+V^2)^{1/2}}{C^2(h+\zeta)^3} - \frac{h+\zeta}{\rho}\frac{\partial p}{\partial y} \tag{16}$$

$$\frac{\partial \zeta}{\partial t} + \frac{\partial U}{\partial x} + \frac{\partial V}{\partial y} = 0 \tag{17}$$

where $U = u(h+\zeta)$ and $V = v(h+\zeta)$ are the depth integrated transport components, t is time, u and v are the vertically averaged velocity components in the x and y directions, g is the acceleration of gravity,

ζ is the sea-level elevation, h is the undisturbed water depth, f is the Coriolis parameter, ρ is the water density, p is the air pressure, and C is the Chezy's friction coefficient (cf. Cunha and Rosman, 2005): $C = 18log\frac{0.37h}{z_0}$, where z_0 is the roughness scale.
The discretized forms for equations 15-17 with the staggered leapfrog scheme (refer to Figure 4) are expressed as:

$$\frac{U_{j,l}^{n+1} - U_{j,l}^{n}}{\Delta t} + \frac{U_{j,l}^{n}}{\overline{\overline{h_{j,l}} + \zeta_{j,l}^{n}}} \frac{U_{j+1,l}^{n} - U_{j-1,l}^{n}}{2\Delta x} + \frac{\overline{\overline{V_{j,l}^{n}}}}{\overline{\overline{h_{j,l}} + \zeta_{j,l}^{n}}} \frac{U_{j,l+1}^{n} - U_{j,l-1}^{n}}{2\Delta y} - f\overline{\overline{V_{j,l}^{n}}} =$$
$$-g(\overline{h_{j,l}} + \overline{\zeta_{j,l}}) \frac{\zeta_{j+1,l}^{n} - \zeta_{j,l}^{n}}{\Delta x} - \frac{gU_{j,l}^{n+1}\sqrt{{U_{j,l}^{n}}^2 + \overline{\overline{V_{j,l}^{n}}}^2}}{\overline{C_{j,l}}^2 (\overline{h_{j,l}} + \overline{\zeta_{j,l}^{n}})^3} - \frac{\overline{h_{j,l}} + \overline{\zeta_{j,l}}}{\rho} \frac{p_{j+1,l}^{n} - p_{j,l}^{n}}{\Delta x} \tag{18}$$

$$\frac{V_{j,l}^{n+1} - V_{j,l}^{n}}{\Delta t} + \frac{\overline{\overline{U_{j,l}^{n}}}}{\overline{\overline{h_{j,l}} + \zeta_{j,l}^{n}}} \frac{V_{j+1,l}^{n} - V_{j-1,l}^{n}}{2\Delta x} + \frac{V_{j,l}^{n}}{\overline{\overline{h_{j,l}} + \zeta_{j,l}^{n}}} \frac{V_{j,l+1}^{n} - V_{j,l-1}^{n}}{2\Delta y} + f\overline{\overline{U_{j,l}^{n}}} =$$
$$-g(\overline{h_{j,l}} + \overline{\zeta_{j,l}}) \frac{\zeta_{j,l}^{n} - \zeta_{j,l-1}^{n}}{\Delta y} - \frac{gV_{j,l}^{n+1}\sqrt{{V_{j,l}^{n}}^2 + \overline{\overline{U_{j,l}^{n}}}^2}}{\overline{C_{j,l}}^2 (\overline{h_{j,l}} + \overline{\zeta_{j,l}^{n}})^3} - \frac{\overline{h_{j,l}} + \overline{\zeta_{j,l}}}{\rho} \frac{p_{j,l}^{n} - p_{j,l-1}^{n}}{\Delta y} \tag{19}$$

$$\frac{\zeta_{j,l}^{n+1} - \zeta_{j,l}^{n}}{\Delta t} + \frac{U_{j,l}^{n+1} - U_{j-1,l}^{n+1}}{\Delta x} + \frac{V_{j,l+1}^{n+1} - V_{j,l}^{n+1}}{\Delta y} = 0 \tag{20}$$

Here $\overline{\overline{V_{j,l}}}$ is the mean of the four grid points surrounding $\overline{\overline{U_{j,l}}}$, and vice versa, and $\overline{h_{j,l}}$ and $\overline{\zeta_{j,l}}$ are the mean of the two grid points, straddling the grid point of $U_{j,l}$ or $V_{j,l}$.

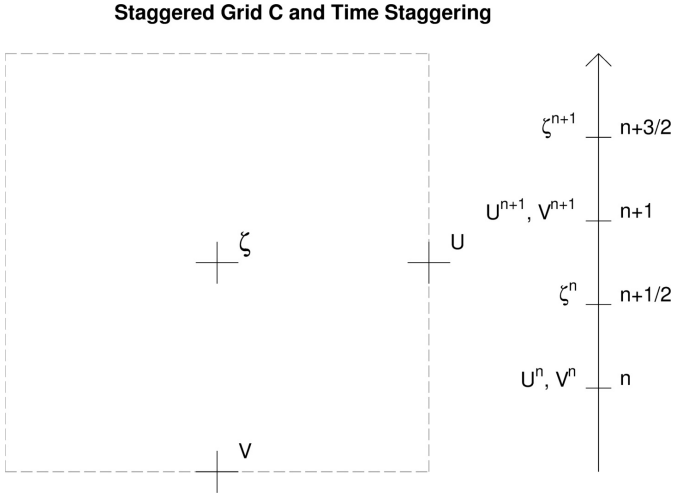

Figure 4: Staggered grid C and time staggering

B.8 Radiation boundary conditions

Orlanski (1984) proposed a radiation scheme in which a local normal phase velocity is computed and used to radiate things out (if it is indeed going out). This works well for a wave propagating normal to the

boundary, but has problems when waves approach the boundary at an angle. Raymond and Kuo (1984) have modified the scheme to account for propagation in all three directions:

$$\frac{\partial \phi}{\partial t} = -(C_x \frac{\partial \phi}{\partial x} + C_y \frac{\partial \phi}{\partial y}) \tag{21}$$

where

$$C_x = F \frac{\partial \phi}{\partial x} [(\frac{\partial \phi}{\partial x})^2 + (\frac{\partial \phi}{\partial y})^2]^{-1} \tag{22}$$

and

$$C_y = F \frac{\partial \phi}{\partial y} [(\frac{\partial \phi}{\partial x})^2 + (\frac{\partial \phi}{\partial y})^2]^{-1} \tag{23}$$

In 22 and 23, $-\partial\phi/\partial t$ has been replaced by F since the general equation describing ϕ can be written formally as

$$\frac{\partial \phi}{\partial t} = -F(x, y, t, \phi, \partial\phi/\partial x, ..., \partial 2^2\phi/\partial x^2, ..., \psi, \chi, ...) \tag{24}$$

Here x and y represent the coordinate directions while $\psi, \chi, ...$ represent other meteorological variables on which ϕ depends.

B.9 Lateral boundary conditions for one-way nested models

One-way lateral boundary conditions are when the host model, with coarser resolution, provides information about the boundary values to the nested model, not being affected by the nested model. "Flow relaxation scheme" is the most widely used scheme for one-way lateral boundary conditions (Kalnay, 2003).
A complete prognostic equation for the regional model near the boundaries can be expressed as:

$$\frac{\partial u}{\partial t} = F - K(u - \bar{u}) \tag{25}$$

where F includes all the regular "forcing terms" in the interior time derivative, and the second term on the right is a Newtonian relaxation term where $\bar{u}$ is solution by the host model.
This equation can be solved numerically using, for example, the leapfrog scheme for the regular terms and backward implicit scheme for the boundary relaxation term, as:

$$\frac{u^{n+1} - u^{n-1}}{2\Delta t} = F^n - K(u_i^{n+1} - \bar{u}^{n+1}) \tag{26}$$

Here the overbar represents the host model, u^{n+1} is the updated regional model, and the subscript i indicates the regional model (internal) solution obtained before relaxing towards the host model values $\bar{u}^{n+1}$:

$$u_i^{n+1} = u^{n-1} + 2\Delta t F^n \tag{27}$$

From (26) and (27) we can now write

$$u^{n+1} = u_i^{n+1} - K2\Delta t u_i^{n+1} + K2\Delta t \bar{u}^{n+1} = (1 - \alpha)u_i^{n+1} + \alpha \bar{u}^{n+1} \tag{28}$$

Here $\alpha = 2\Delta t K$ varies from 0 in the interior ($K = 0$), to 1 at the boundary, where the regional model solution is specified to coincide with the host model solution.

C Data and Methods

For this study, we used the 1-min sea level data of the Korea Hydrographic and Oceanographic Administration (KHOA) from 22 tide sites along the west coast of South Korea (Table 2).

Table 2: Tidal site locations and available years of the used data.

Site					Year											
ID	Name	Full name	Lat.	Lon.	02	03	04	05	06	07	08	09	10	11	12	13
1	AH	Anheung	36.67	126.13	x	x	x	x	x	x	x	x	x	x	x	x
2	AS	Ansan	37.19	126.65	x	x	x	x	x	x	x	x	x	x	x	x
3	BR	Boryeong	36.41	126.49	x	x	x	x	x	x	x	x	x	x	x	x
4	CJ	Chujado	33.96	126.3	x	x	x	x	x	x	x	x	x	x	x	x
5	DS	Daesan	37.01	126.35		x	x	x	x	x	x	x	x	x	x	x
6	EC	Eocheongdo	36.12	125.98							x	x	x	x	x	x
7	GE	Guleopdo	37.19	125.00								x	x	x	x	x
8	GH	Ganghwadaegyo	37.73	126.52						x	x	x	x	x	x	x
9	GS	Gunsan	35.98	126.56	x	x	x	x	x	x	x	x	x	x	x	x
10	HS	Heuksando	34.68	125.44	x	x	x	x	x	x	x	x	x	x	x	x
11	IC	Incheon	37.45	126.59	x	x	x	x	x	x	x	x	x	x	x	x
12	JD	Jindo	34.38	126.31					x	x	x	x	x	x	x	x
13	JH	Janghang	36.01	126.69			x	x	x	x	x	x	x	x	x	x
14	MP	Mokpo	34.78	126.38	x	x	x	x	x	x	x	x	x	x	x	x
15	PT	Pyeongtaek	36.97	126.82	x	x	x	x	x	x	x	x	x	x	x	x
16	SC	Seocheonmaryang	36.13	126.50										x	x	x
17	SD	Incheonsongdo	37.34	126.59										x	x	x
18	TA	Taean	36.91	126.24										x	x	x
19	WD	Wido	35.62	126.31	x	x	x	x	x	x	x	x	x	x		
20	YG	Yeonggwang	35.43	126.42	x	x	x	x	x	x	x	x	x	x	x	x
21	YH	Yeongheungdo	37.24	126.43									x	x	x	x
22	YJ	Yeonggongdaegyo	37.55	126.58									x	x	x	x

In deciding what should be considered as a meteorological tsunami event, it would be a matter of choice of criteria. Possible criteria may include absolute wave height and relative wave height. The latter considers different levels of background noise by site (Monserrat et al., 2006). Šepić et al. (2012) and Rabinovich and Monserrat (1996) chose residual sea level height of 25 cm and 30 cm respectively as the threshold. The KMA counted it as event day when at least three neighbouring sites exceeded their critical value of the 95% confidence level of amplitude of waves during the same time period (KMA, 2013). Based on this, the KMA (KMA, 2013) documented a total number of 49 tsunami-like sea level oscillation events in spring (March-May) between 2002 and 2013 (Table 3). We used the KMA results for this study.
The figures show that: (i) tsunami-like sea level oscillations are recorded at the 10 sites among 22 sites, (ii) the total event mean sea level is 21.5 cm, (iii) maximum sea level is 131.7 cm at YG (Event 15), and (iv) mean sea level by site ranges from 9.8 cm (BR) to 31.6 cm (YG). It is also featured that YG has no event since the last one in 2009, and event most frequently occurs at HS and EC. These points will be further discussed in the following sections.

Table 3: Minimum or maximum values of sea level during the meteotsunami events

No.	Time of Max	YG	MP	GS	CJ	JH	BR	WD	AH	HS	EC	Sig. level
critical value (2σ)		15.9	14.3	12.3	10.9	19.6	6.4	12.9	17.9	12.9	6.4	
critical value (3σ)		20.9	18.8	16.2	14.4	25.7	8.4	17	23.5	16.9	8.4	
1	21.03.2002 03:34	-25.2		-17.0			7.8	15.1	21.4	16.4		0.95
2	16.04.2002 11:10	-27.3		25.7			-8.3	18.1	-22.6	-13.7		0.99
3	25.04.2003 04:56	-29.6		25.6					34.4			0.99
4	17.03.2004 13:23	18.7	-16.2	-14.2	14.3							0.95
5	24.04.2004 14:05		17.5		14.5		-6.6					0.95
6	11.05.2004 19:03	-17.2		12.4	-13							0.95
7	11.03.2005 04:48	19.4		18.9			6.5					0.95
8	22.03.2005 21:54	-18.4	-20.2		11.9							0.95
9	24.03.2005 12:57	24.2			-13.1		-9.3					0.95
10	19.04.2005 23:34			-25			-9.9			-16.2		0.95
11	20.04.2005 01:49			39.8		29.9	-19		36.3	27.3		0.99
12	19.04.2006 08:12			-31.7			-18.9	33.4	24.3			0.99
13	05.03.2007 09:56				12.8			-15.3		15.6		0.95
14	29.03.2007 18:25	39.3		23.6				42.1		16.9		0.99
15	31.03.2007 01:40	131.7		59.5	13.3	40.5	14.9	131.3	-70.2	-53.9		0.99
16	01.04.2007 07:22				-23.4			-14.9		27.1		0.95
17	09.05.2007 16:26	-23.5		-14	-20.8			21.5	-24.6	-19.8		0.99
18	25.04.2008 22:30	-31.2			19	-21.6	6.7	-13.2	21.6	-23	10.4	0.99
19	04.05.2008 11:48	18.4						19.7		-14.8	9.9	0.95
20	17.05.2008 17:12	19.7						-13.3		21.8	-7.8	0.95
21	18.05.2008 14:18							-13.3		-13.5	6.5	0.95
22	15.04.2009 15:39	-38.1		15.3					42.1	30.9	-27.5	0.99
23	16.05.2009 03:30	-23.5						14.3		-21.3		0.95
24	01.03.2010 06:58				22.5		6.7			-15	19.7	0.95
25	03.03.2010 11:44				12.4					-13.1	-7.9	0.95
26	05.03.2010 10:06				17.9					-19.5	8.5	0.99
27	06.03.2010 13:42				12.4					17.7	-10.2	0.95
28	20.03.2010 14:13						7.4	21.7		-13.2	20.3	0.95
29	22.03.2010 19:17				18.5					19.1	-7.1	0.95
30	25.03.2010 05:07				15.2					-24.7	-7.8	0.95
31	10.04.2010 23:23				-13.3			14.4			-14.5	0.95
32	11.04.2010 04:41							-15.3		-15.8	-14.6	0.95
33	21.04.2010 18:36			17.7	12.2		8.2		-18.2	13.4	17.5	0.95
34	27.04.2010 04:34							34.6		15.4	18.6	0.95
35	24.05.2010 16:45				-15.1			18		-39.3	-11.2	0.99
36	11.04.2011 02:04							-16.2		-13.5	13.7	0.95
37	25.04.2011 23:55				11			-23.3		13	-14.5	0.95
38	26.04.2011 11:05				-24.3			23.2		-76.5	-24.2	0.99
39	30.04.2011 19:13				-11.5		-9.1	25.8	21.6	-23.2	23.7	0.99
40	08.05.2011 19:56						-7.2		-26.2		10.6	0.95
41	20.05.2011 18:09						9.1	13.1			22.1	0.95
42	21.05.2011 17:46			-15.2			-10.4	-18.5	19.8	13.4	-25.4	0.99
43	03.03.2012 16:48				-15.2					-17.3	-7.5	0.95
44	03.04.2012 04:52				19.9					-14.2	8	0.95
45	16.05.2012 20:35							-13.3		-15.3	-9.5	0.95
46	09.03.2013 21:26							21.1		-14.4	-7.2	0.95
47	13.03.2013 02:14				15			17.3		21.4	-12.5	0.99
48	22.03.2013 12:06				-12.1					13	-7.4	0.95
49	14.04.2013 06:52			-12.8	11.9			17.9	-20.3	14.7	20.9	0.95
No. of event		16	3	16	27	3	17	28	14	38	31	
Average height		31.6	18	23	15.4	30.7	9.8	23.5	28.8	20.7	13.8	21.5

We filtered the tide time series with high-pass Butterworth window (Emery and Thomson, 2004) to remove period components longer than 2 h, followed by wavelet analysis. We used the Morlet as the basis wavelet. We estimated the arrival time of the maximum amplitude for each event from the wavelet analysis. These times are considered as peak times of the events, and used as the basis point for analyses.
For the analysis of atmospheric disturbances during the events, we used the KMA 1-min MSLP data from the 64 sites of west coast (Figure 5). Same methods for filtering and spectra analysis were used for the pressure data.

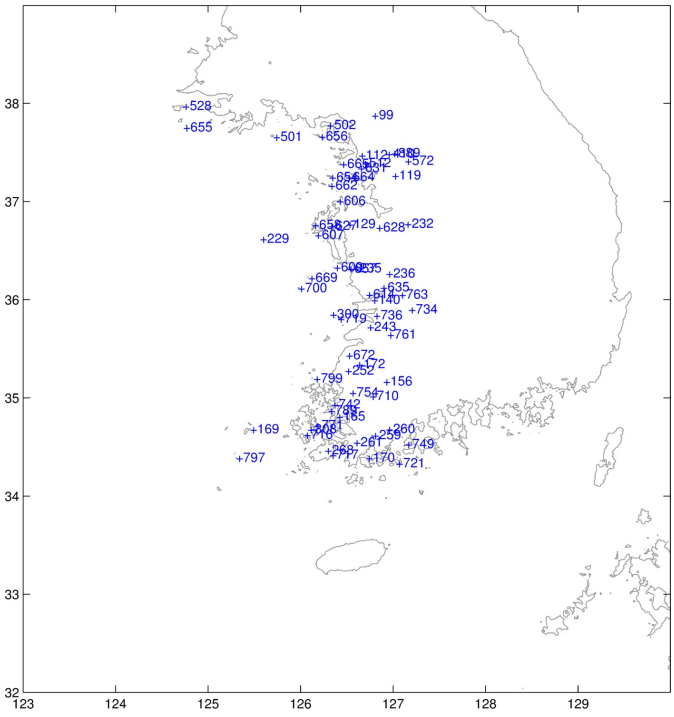

Figure 5: Locations of the MSLP sites whose data were used for this study. Numbers indicate site IDs.

For synoptic analysis, we used ECMWF's ERA-Interim synoptic monthly mean and 6-hourly surface and upper level reanalysis data over the East Asia (20-60°N, 90-150°E) with 0.75×0.75° resolution. Parameters includes mean sea level pressure (MSLP), 2-m temperature, 10-m wind, and temperature, geopotential, relative vorticity and wind at the levels of 850 hPa, 700 hPa, 500 hPa and 300 hPa. In addition, 23 level data from 1000 hPa to 200 hPa were used for vertical profiles over the Yellow Sea.
We constructed data fields of the variables at the peak time of sea level oscillation per each event from the reanalysis data by linear interpolation. Event peak average fields for all the variables were compared with spring (March-May) mean fields between 2002 and 2013 to identify characteristics of favourable synoptic setting for meteotsunamis. In addition, normalized event mean fields were also made for this purpose. To remove synoptic climate signal, we normalized the time series at each grid point, by subtracting spring mean (March-May) over the period of 2002-2013 from the time series, and dividing it by the standard deviation of the the anomaly. In addition, we made interpolated 1-hourly fields for 12 hours before and after the event peak times to examine the evolution of variables. We derived EOFs or PCs, that explain the most of variance of the variables.
Finally, we conducted numerical experiments based on the spectral analysis of tide and pressure.

D Results

D.1 Synoptic Analysis

Forecasters may first eager to know the favourable synoptic conditions under which meteotsunami may more favourably occur. As discussed at the introduction, 53% of meteotsunami events occurred in spring during 2002-2013 (KMA, 2013). This suggests that the synoptic background in spring is more favourable than in other seasons for meteotsunami outbreak.

D.1.1 Analysis of event mean

Three major levels

The spring (March-May) mean weather charts over the East Asia for the period of 2002-2013 are compared with the event mean charts of the peak times (Figure 6). The spring mean surface chart (a1) is featured that the southern Yellow Sea and northern East China Sea region is under a weak anticyclone surrounded by the four air masses, cP (continental polar) to the north-west, mT (maritime tropical) to the south-east, cT (continental tropical) to the south-west and mP (maritime polar) to the north-east. The event mean surface chart (b1) shows that all the air masses are intensified in some extends, expanding to the Yellow Sea region, and the Korea Peninsula is covered by a low pressure system. The main core of the jet stream is along the south coast of Japan in the spring mean (a3), whereas the northern jet streak is developed, and meanders around 45N in the event mean (b3). A strong positive relative vorticity max is located over the Manchuria region at the level of 500 hPa (b2), which may further develops the surface low.

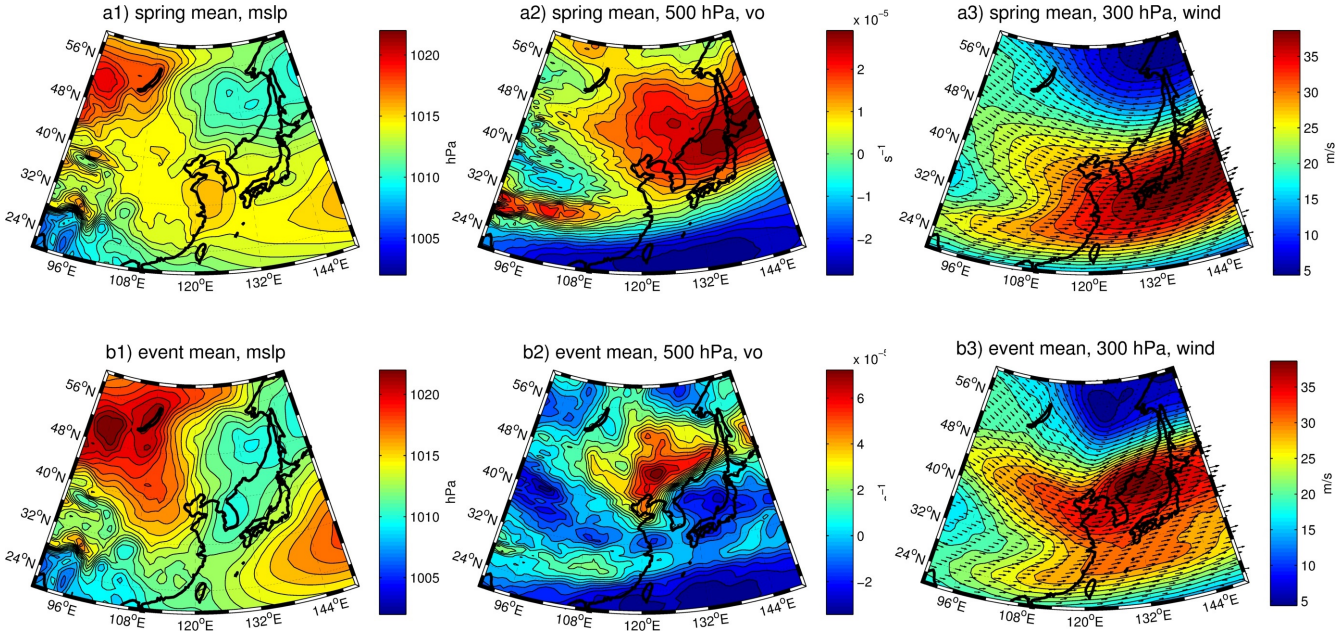

Figure 6: Mean sea level pressure (1), 500 hPa relative vorticity (2), and 300 hPa wind (3) of the spring (March-May) mean (a) and event mean (b) at the peak times of the meteotsunamis.

Vertical profiles

Figure 7 presents the meridional cross section charts of 124E over the Yellow Sea. The most prominent feature of the vertical profiles is that the wind isotachs of the event mean are displaced downward (low

level jet streams), and the jet stream core is extended up to the north (b2) compared to the spring mean (b1), which is line line with the cores of the anomalies of pressure gradient, wind speed, temperature and relative vorticity, which are tilted northwards as level goes up. Wind maxima are located at a near-surface level, 600 hPa and 300 hPa over 33N, 35N and 42N respectively (b3). An extended temperature inversion layer, centred at 29N, forms up to the level of 850 hPa (c3), which is related with the decreased 100-500 hPa thickness over 35N (a3). Also there exists a temperature version layer at the level of about 500 hPa over 35N (c3). Positive vorticity cores are positioned at the levels of about 900 hPa and 600 hPa over 35N and 38N respectively (d3).

Literature indicates that vertical profiles of atmosphere over an area where significant air pressure oscillations occur are often characterized by temperature inversion in the lower 2000 m, presence of an unstable air between 4000 m (600 hPa) and 6000 m (400 hPa) and a wind maximum at approximately 5000 m (500 hPa) (Monserrat and Thorpe (1992), Monserrat (1996), Vilibić and Šepic (2009)). From the vertical profiles we can see all of such properties.

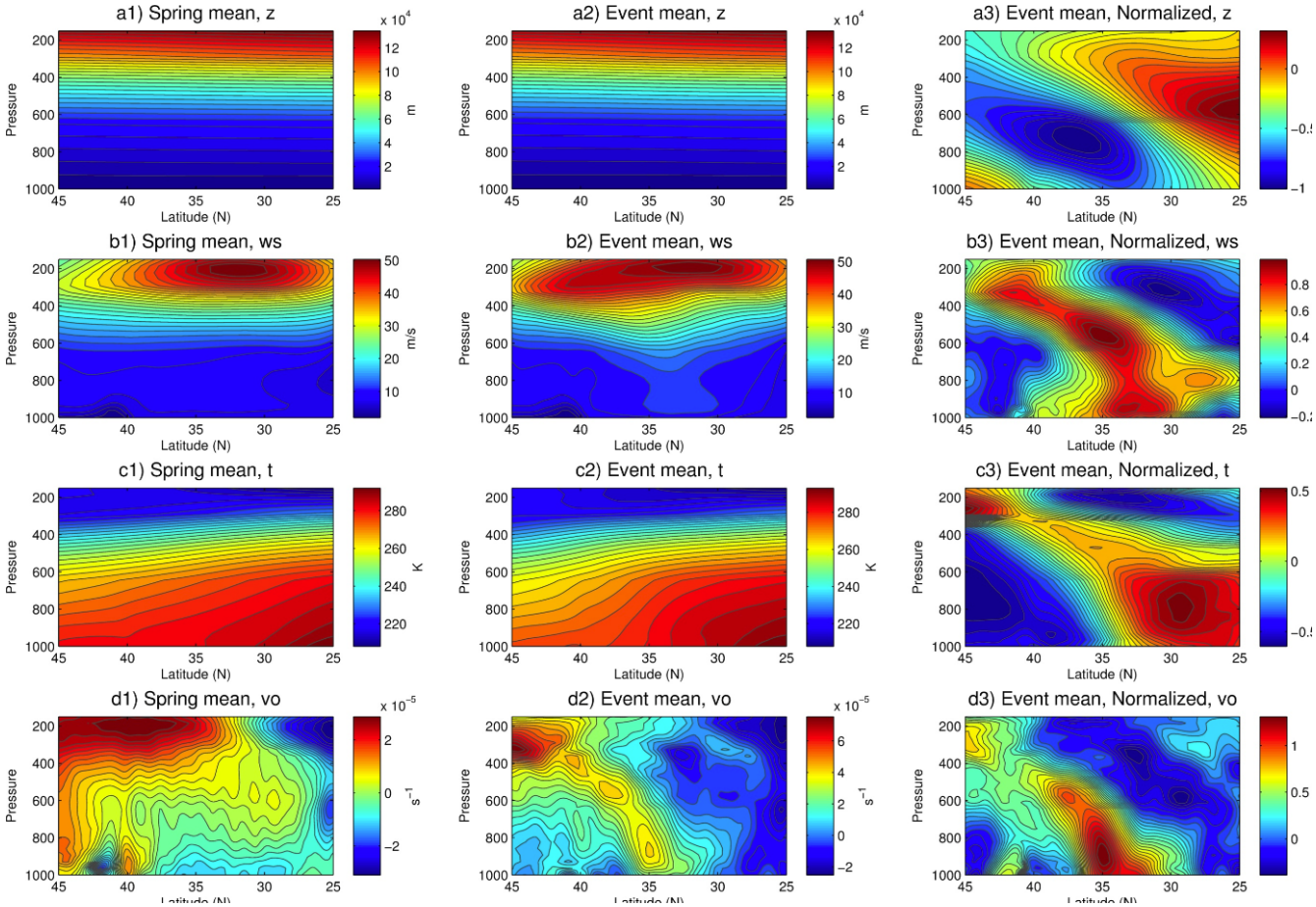

Figure 7: Same with Figure 6 but for meridional cross section of 124E: geopotential height (a), wind speed (b), temperature (c) and relative vorticity (c) for the spring mean (1), event mean (2) and normalized event mean (3).

Change of surface pressure fields

Figure 8 shows the change of MSLP mean with 6 hour increments from 24 hours before to 24 hours after the peak times of the events. The cT is the most dominant system 24 hours before to the Yellow Sea area. However it shrinks, as the cP and mT expands, and the mP appears to suck up the remaining low pressure over the Yellow Sea that seems to stem from the cT from 6-h before to 6-h after the peak time. By examining each case, it turns out that the main patterns of surface atmospheric pressure movement are from the north-west and from the south-west.

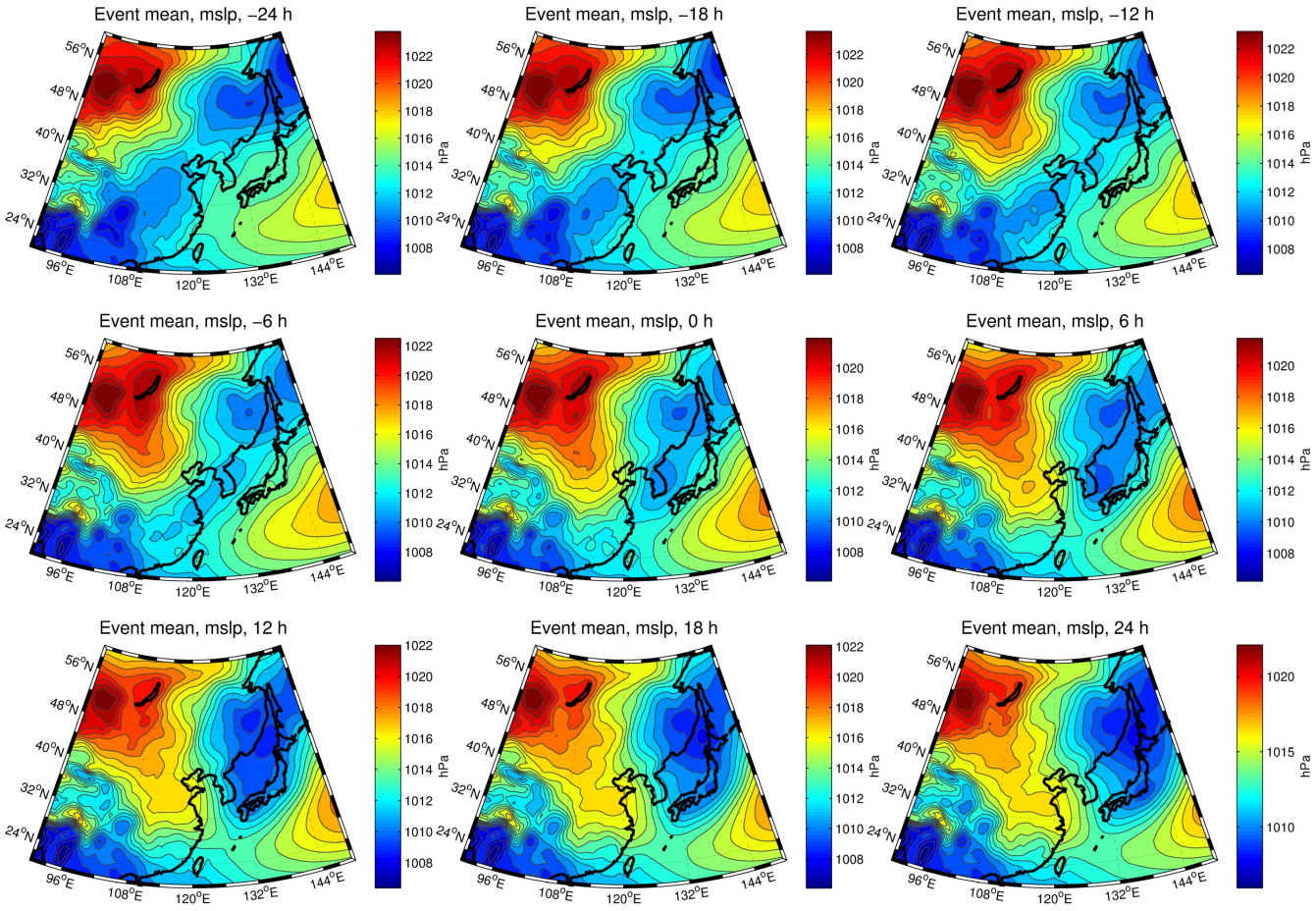

Figure 8: Change of event mean surface pressure field for 2 days centred at the peak times of meteotsunamis for March-May in 2002-2013.

D.1.2 EOF analysis

We performed the EOF analysis for the variables at some major levels. Here we present one for MSLP charts (Figure 9) taken at the peak times of the events. The mP and cT (lows), expanding south-westward and north-eastward respectively (a), make minus anomaly over the Korea Peninsula (b) (compare with the spring mean in Figure 6). Next shown are the two EOFs (1), the expansion coefficient of EOF for the events (2), and most relevant event to each EOF with positive expansion coefficient (3).
The EOF analysis reveals two main patterns of MSLP, which account for 57.1 % of the total variance. The first mode illustrates that the Yellow Sea region is over in between a high (or low) and a low (or

high) at the peak time. The second EOF depicts that the Korea Peninsula is covered by a big low (or high) whose center is located over Baekdu (the border of North Korea and China).
Interpretation on the physical meanings of the EOFs will be given in Section E.

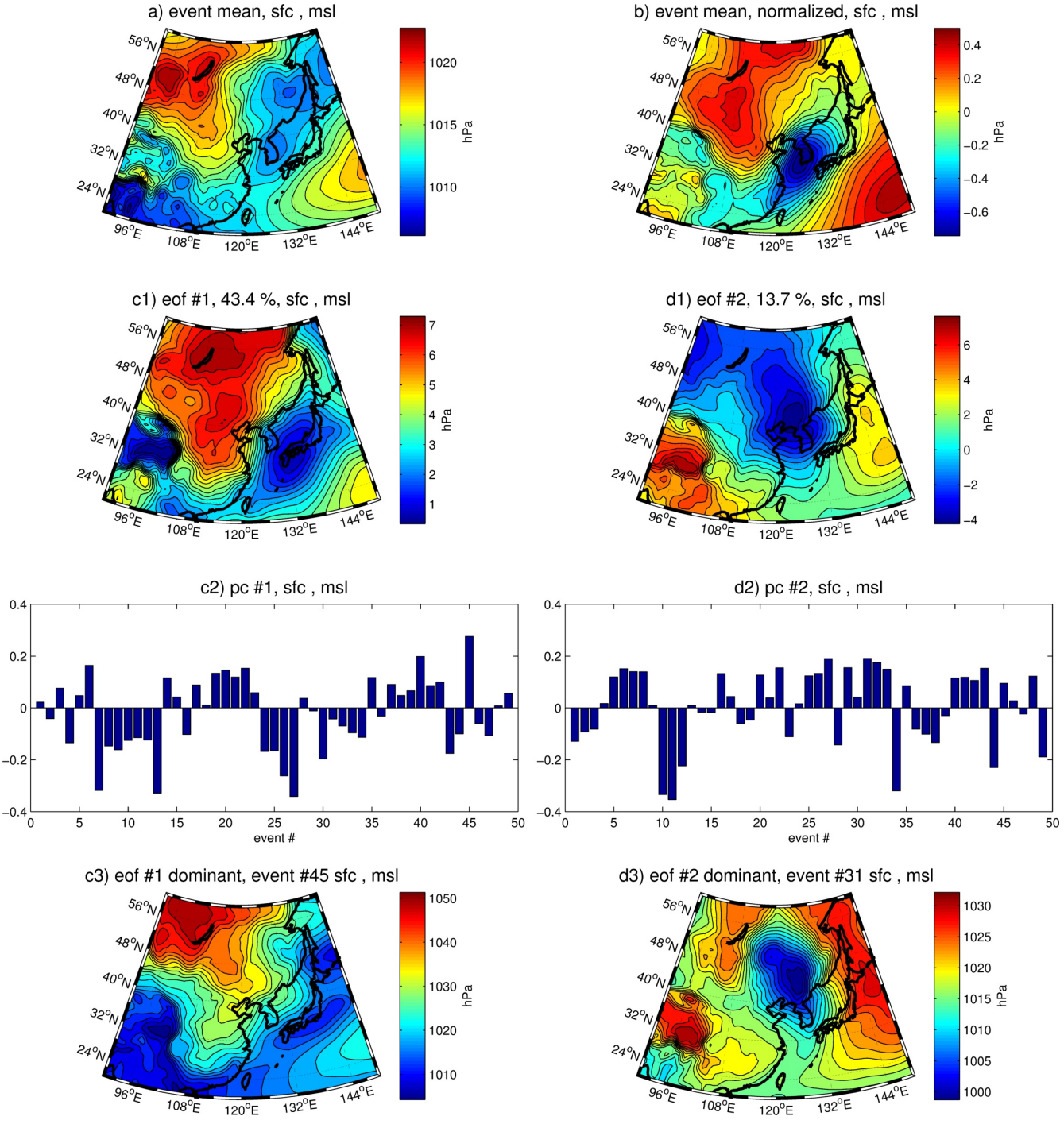

Figure 9: Result of MSLP EOF analysis: a) event mean, b) its anomaly mean, 1) the two EOFs, 2) expansion coefficient for each EOF, 3) and the most relevant event to each EOF with positive expansion coefficient.

D.2 Spectral Analysis

To find properties of the long ocean waves and the atmospheric disturbances during the events, we conducted wavelet analysis of the sea level time series for the all events, and MSLP time series for Events 13-49. MSLP and sea level time series centred at the peak times were filtered with a 2-h high-pass Butterworth window, and wavelet analysis was performed. Figure 10 shows locations of tide and MSLP sites (left panels), and wavelet power spectra (right panels) of a tide and a MSLP site, which are close to each other. The thick contour encloses regions of greater than 99 % confidence for a red-noise process with a lag-1 coefficient of 0.77 (2). The dashed line indicates 99 % confidence level (3 and 4). We may consider the time with the maximum scale-averaged wavelet power (4) as the arrival time of long ocean waves or a pressure disturbance at a certain site. Hereinafter the same criteria are applied to the other wavelet power spectra unless otherwise mentioned.

It is noted that the changes of energy of the two signals are quite in line, and the peak times are close to each other. Even though there exists a coincidence in energy changes in time, dominant periods are different. The sea level global wavelet spectrum shows some prominent peaks, while at the MSLP spectrum peaks are not so outstanding. It explains that in some sites, the periods of the sea level oscillations are predetermined by the resonant properties of the site (natural resonant periods). These characteristics commonly appear most of the sea level sites because they are all located in bays/harbours/inlets with natural periods (refer to Figure 11).

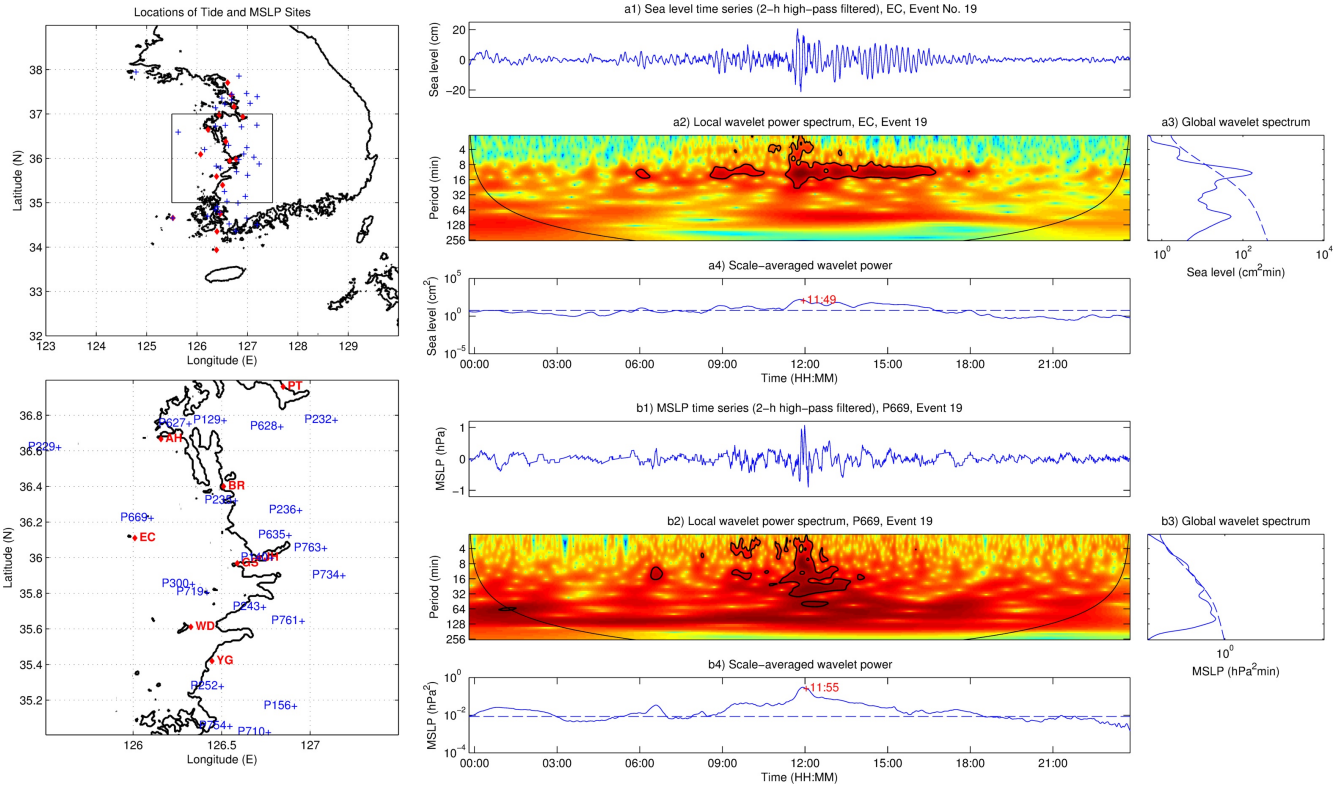

Figure 10: a) Sea level and b) MSLP 2-h high-pass filtered 1) time series and their 2-4) wavelet power spectra for Event 19.

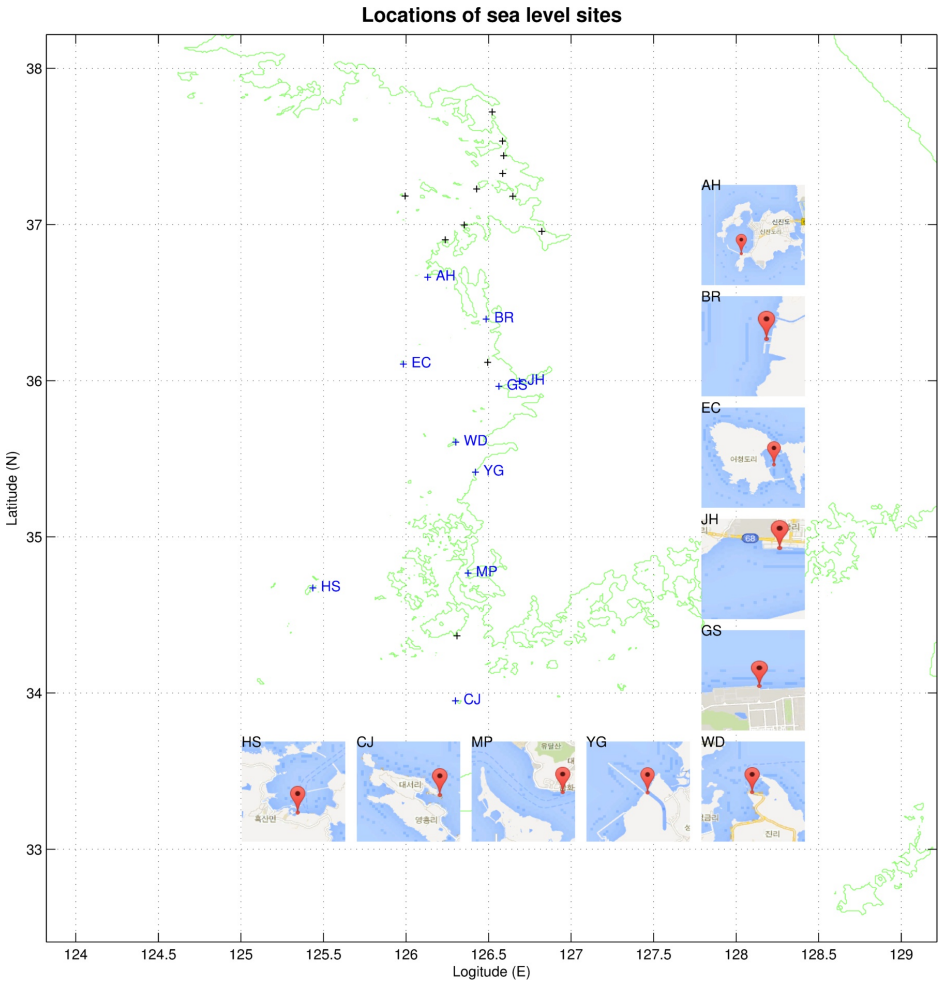

Figure 11: Locations of sea level sites. The width of the site pictures is equivalent to about 3 km.

Sea level spectral analysis

To figure out mean characteristics of sea level oscillations at each site during the events, we constructed global wavelet spectra for the background mean (blue) and the event mean (red), which were taken by averaging the global wavelet spectra for 48 hours and 6 hours centred at the peak times respectively during the events (Figure 12). The numbers indicates energy gain, which is defined as square root of the cumulative event mean over background mean energies. The gain may represent the amplification factor due to the obtained energies from the atmospheric disturbances during the events.
The main feature is that high-frequency waves (periods of 2.5-4.8 min) are excited at all the sites except for GS. This is because these sites are positioned in harbours/bays/inlets, whereas GS is open to ocean (see Figure 11). This frequency band (periods of 2-4 min) may be more associated with harbour resonance, while the low frequency band (periods of 8-128 min) may be more related with self effect and seiche activity along coastline. Comparing the mean wave heights at the sites (see Table 3), and taking into account the cumulative energy ratio, it is noted that the more higher frequencies are dominant, the higher waves are generated. The sites may be categorized into three groups; (i) JH, GS, WD, YG and AH, which have high gains (1.9-2.2) and high sea levels (23.0-31.6 cm), (ii) CJ and EC, which have high gains (2.3-2.5) but low sea levels (13.8-15.4 cm), and (iii) HS, MP and BR, which have low gains (0.5-1.1) with varying sea levels (9.8-20.7 cm). The main difference between the groups (i) and (ii) is that waves at the periods of 8-64 min are more pronounced for the first group than for the second group. This may be because the

second group has much narrower shelves than the first group (islands). Energy convergence at the period of about 16 min at HS, which is a relatively big island, may be related with shelf effect, which results in higher sea level (20.7 cm). MP (18 cm) may do not have shelf effect because waves decay while passing the archipelago. BR (9.8 cm) is protected by the Taean Peninsula and nearby islands (see next section).

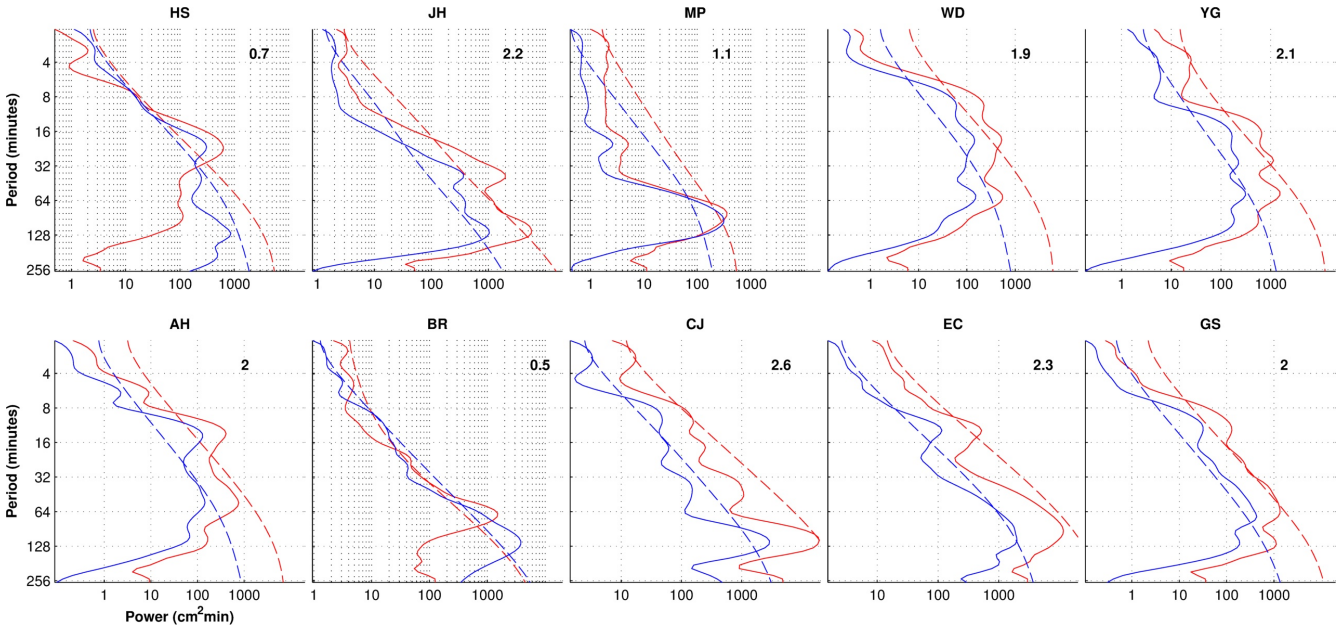

Figure 12: Background mean (blue) and event mean (red) global wavelet spectra of sea levels at the sites after a filtering with 2-h Butterworth window. The dashed lines indicate 99% confidence level and the numbers are the ratio of cumulative energy between the event mean and the background mean.

From the wavelet spectra, natural modes of each event site were identified (Table 4).

Table 4: Natural periods of the event sites

Site	Natural period (min)
HS	3.1, 21.8
JH	3.1, 38.0
MP	2.9, 20.3
WD	2.5, 9.4, 19.0, 61.7
YG	3.9, 16.5, 28.8, 57.6
AH	5.8, 13.4, 53.7
BR	2.5, 5.1 23.3
CJ	2.9, 10.9, 17.7, 46.8
EC	4.7, 12.5
GS	12.5

MSLP spectral analysis

To identify features of dominant periods of the atmospheric disturbances during the meteotsunami events, we further conducted wavelet power spectral analysis for the MSLP time series from the coastal sites for the events in a similar way. To extract time series with pressure jumps, we applied the procedures for

pressure jump, which is defined by the KMA as air pressure changes of more than 3 hPa for an hour and calculated as follows:

(i) De-trended time series are smoothed by taking 10-minute moving mean:$p_{10min}(i) = \frac{\sum_{t-5}^{t+4} p_{t=i}}{10}$
(ii) 1-h pressure jump is calculated by: $p_{1h}(i) = max(p_{1hrange}(i)) - min(p_{1hrange}(i))$
(iii) Classified as a pressure jump when a value is more than 3 hPa.

We examined the MSLP time series from coastal areas for 2006-2013 (Events 12-49), and selected an MSLP time series with pressure jumps, representing each event, which is most likely associated with the event. Then we located the timing of the maximum of pressure jump for 1 h, which is considered as peak time of the atmospheric disturbance.
Then we examined the pressure series to categorize the pressure disturbances by shape, which is related with energy transfer efficiency to long ocean waves (Figure 13). It turns out that in most cases, the pressure series have cosine-type pressure disturbance, featured by a fluctuation of pressure with or without periods (a and b). However box-type pressure jumps, characterised by a very sharp increase (or decrease) of pressure, are rare (c) (in case of Event 15, a box-type disturbance is followed by a cosine-type disturbance). In addition, it reveals that in average, the duration of the disturbances is about 3-4 h, varying from 2 to 9 h.

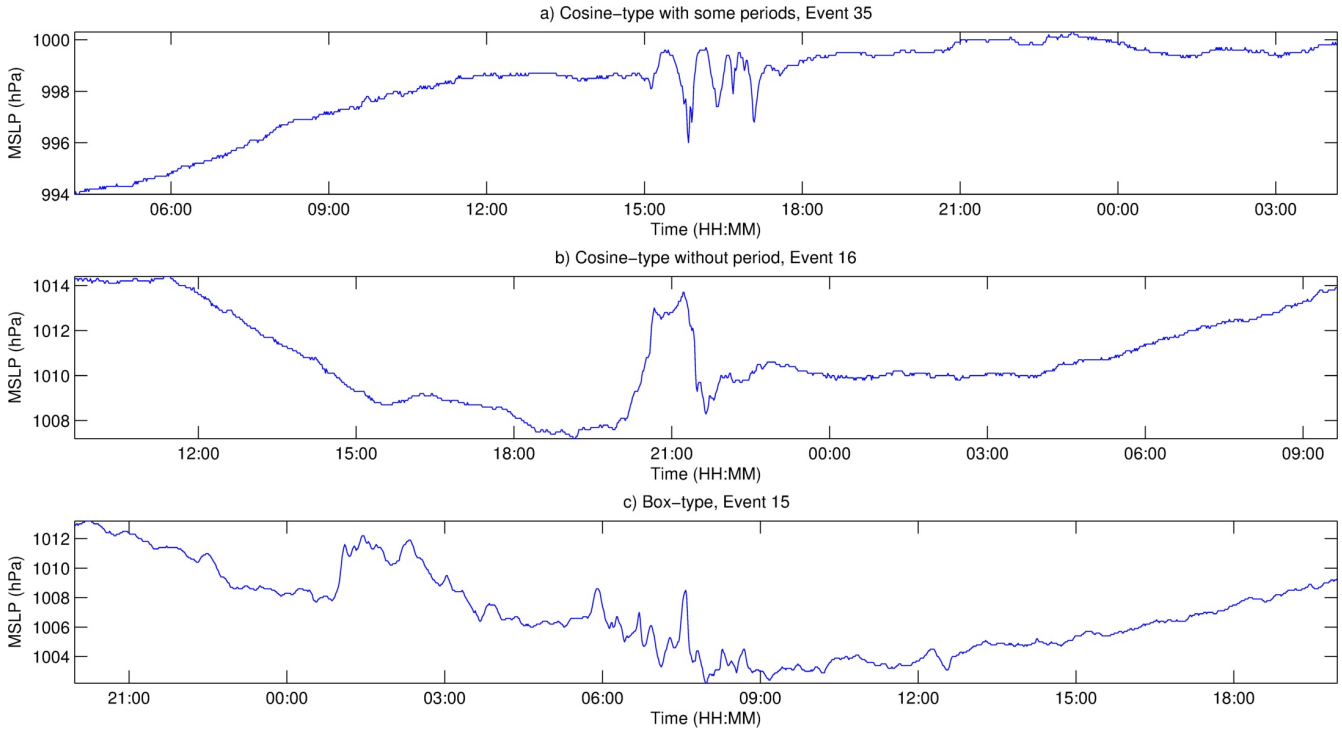

Figure 13: Types of atmospheric disturbances by shape: a) cosine-type with periods, b) cosine-type without period c) and box-type.

To analyse scales of the atmospheric disturbances, using the 37 time series, we extracted pressure jump maxima for different time ranges during a period of 6 hours centred at the peak time for each event (Figure 14). The event mean pressure jumps for 128, 64, 32, 16, 8, 4 and 2 min are 4.2, 3.6, 3.3, 2.6, 1.9, 1.2 and 0.5 hPa respectively. The 32 min and 4 min ranges are highlighted in thick lines, which are associated with the periods of harbour and shelf resonance of most sites (refer to Figure 12 and Table 4).

The pressure jump maxima at these periods are significantly high at Event 15, which is engaged in severe damages to Youngwang (related site: YG). On the other hand, the maxima for the other event with damages, Events 19 (related sites: GS, EC and BR) and 38 (related site: HS) are not outstanding. Since HS has a narrow band spectrum, we can guess that the damages at HS would be related with harbour resonance at its natural periods. However, in case of Event 19, there seems no common factors that are possibly blamed for the damages so far. We will discuss this point further in Section E.

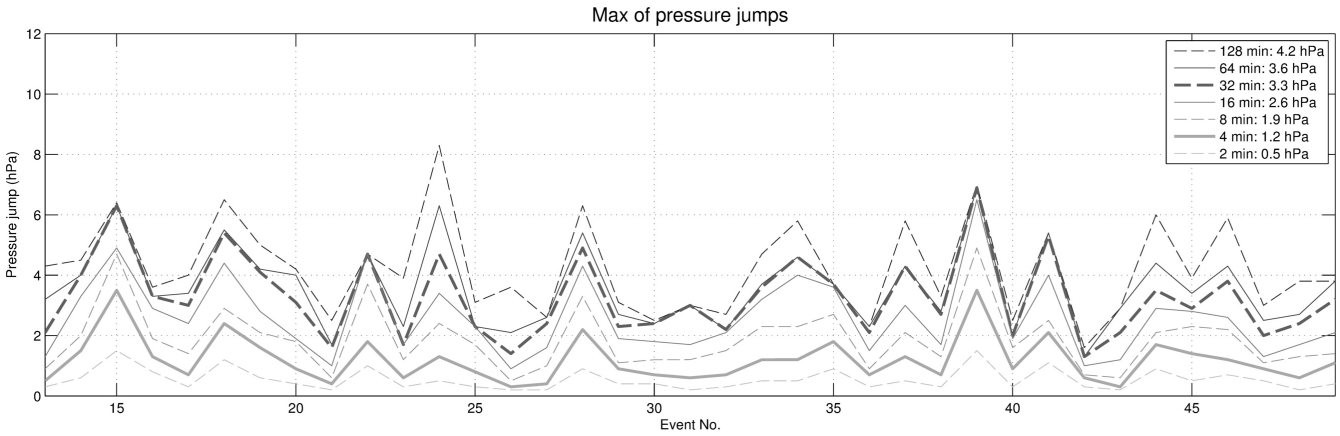

Figure 14: Pressure jump maxima for different time ranges for Events 13-49. Mean values for each time range are given in the legend.

Based on the peak times, we formed global wavelet spectra of 2-h high-pass filtered time series in the same way but for 72 hours for the background mean and 6 hours for the event mean (Figure 15). It shows that the dominant periods of pressure waves are not pronounced as they have been smoothed out by averaging. Even though they are not pronounced, there are two peaks at 16.5 and 57.6 min. This may imply that disturbances at these periods are most persistent during the events.

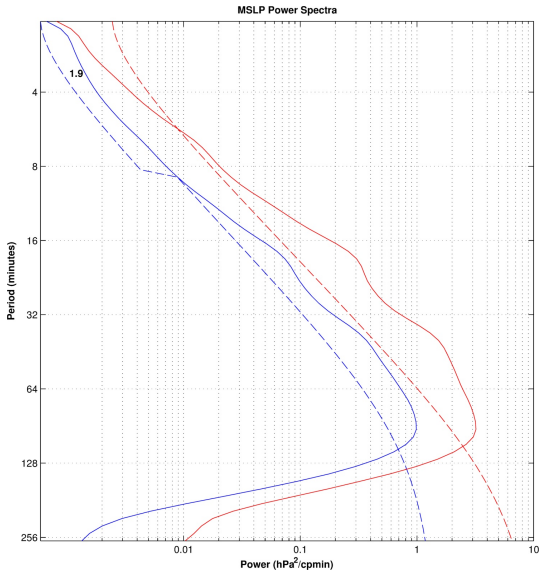

Figure 15: Same as Figure 12 but for the pressure disturbances during 37 events between 2006 and 2013.

The KMA (KMA, 2013) estimated velocities of the 26 atmospheric disturbance cases in spring (Mar-May) between 2006 and 2014 based on the above-mentioned procedures for pressure jump and isochronal methods, using the MSLP data from the sites along the west coast. The results are reproduced in Figure 16. It reveals that the mean pressure jump is 3.5 hPa, and the mean velocity is 31.1 m/s (arithmetic) from 277.5^o (median). The main feature is that there are two patterns of direction, from the north-west and the south-west. If we divide them into two groups based on 270^o, the medians of the groups are 321.5^o, and 230.0^o respectively. Both groups have the same mean intensity (pressure jump of 3.5 hPa for 1 hour), but the mean speed of the SW group (45.6 m/s) is much faster than the NW group (20.4 m/s). This point will be a little bit more discussed later. As for frequency, 14 samples belong to the NW group, and 12 to the SW group.

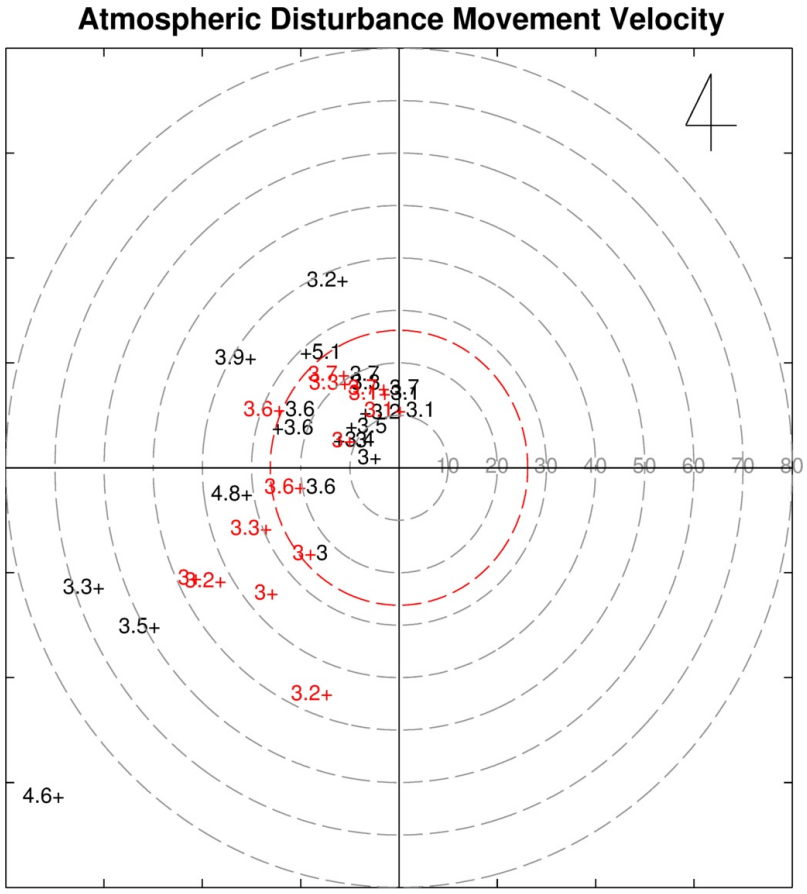

Figure 16: Pressure jump movement velocities for the 26 cases in spring between 2002 and 2014 (after KMA (2013)). The numbers indicate pressure change for 1 h (event-related cases are in red). The red circle indicates the speed, 26.2 m/s, the most probable speed for Proudman resonance over the Yellow Sea.

We find that among the 26 cases, 14 cases are related with the meteotsunami events (see Table 5). This means that some pressure disturbances did not cause meteotsunami. The reasons for that may include: speed of disturbance being out of range of the Proudman resonance, too short movement distance for generation of resonances, and errors in estimation.

Table 5: Estimated velocities of 1-h pressure jumps in spring during 2006-2014, which are related with the mteteotsunami events (after KMA (2013)).

Event No.	Date	1-h pressure jump (hPa)	Speed (m/s)	Direction(degrees)
14	28 Mar 2007	3.3	20.5	323
15	30 Mar 2007	3.7	21.9	325
18	25 Apr 2008	3.1	11.2	355
19	04 May 2008	3.0	12.5	296
20	17 May 2008	3.6	21.6	261
22	15 Apr 2009	3.1	15.0	344
24	01 Mar 2010	3.0	47.4	244
28	20 Mar 2010	3.2	45.7	200
37	25 Apr 2011	3.0	25.1	230
39	30 Apr 2011	3.6	28.0	294
41	20 May 2011	3.2	43.2	240
42	21 May 2011	3.3	30.5	248
44	03 Apr 2012	3.0	35.9	229
46	09 Mar 2013	3.7	16.0	344
Mean		3.8	26.8	278

Looking at the bathymetric map of the Yellow Sea (Figure 17), the Proudman resonance would take place over the slowly varying depth zone, surrounded by 60 m contour line, varying from 60-80 m. This implies that the Proudman resonance may be most likely generated by a disturbance with a speed of 26.2 m/s ($c = \sqrt{70 \times 9.8}$). The results of the atmospheric disturbance velocities support that the tide sites without any meteotsunami event are positioned at relatively safe places from the long ocean waves approaching from the north-west and the south-west. The high frequencies of occurrence at EC and HS are due to the fact that these two sites are open to long ocean waves coming from both directions. In addition, we can see that the reason of no event at YG since 2010 should be related with the construction of the sea wall (refer to Figure 11) and the increasing number of atmospheric disturbances from the south-west (refer to Table 5).

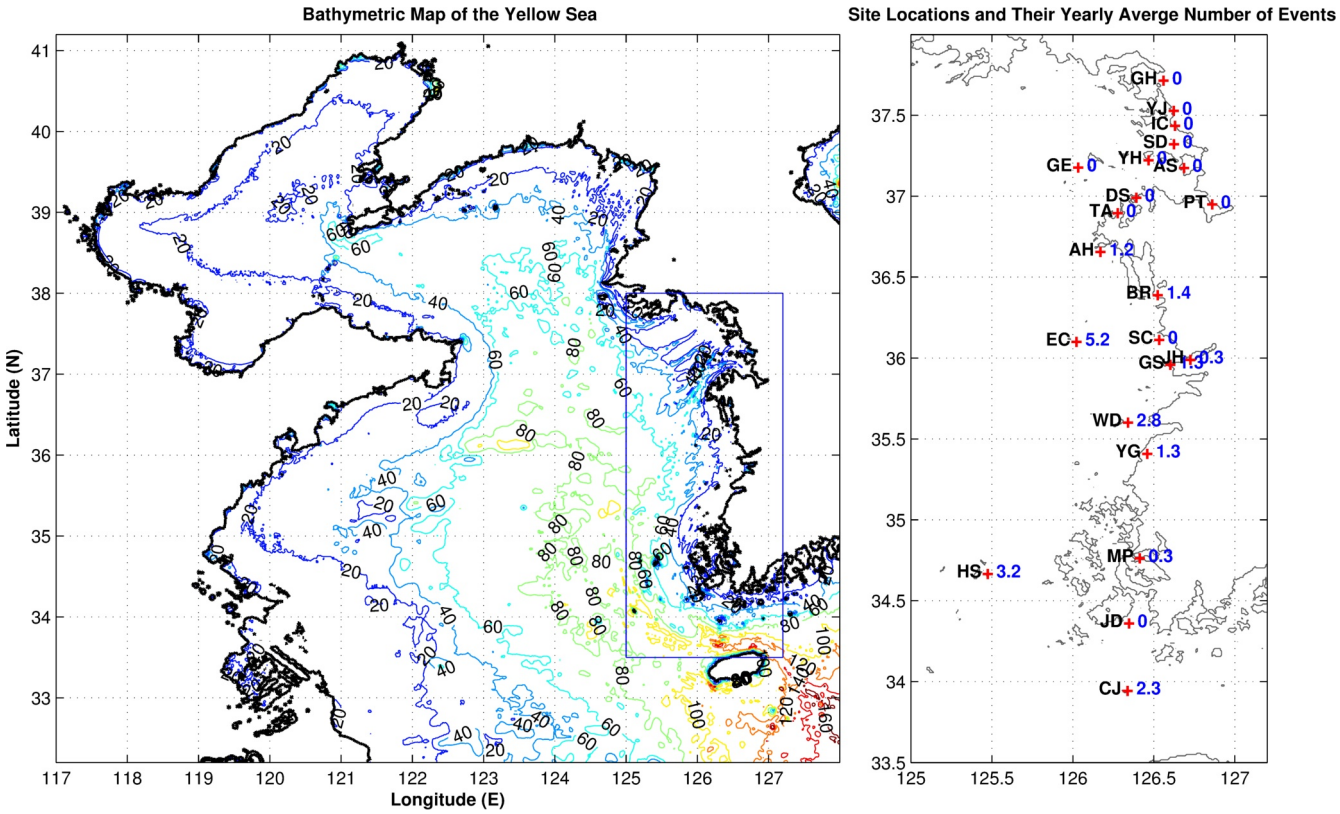

Figure 17: Bathymetric map of the Yellow Sea (left) and sea level site locations and their yearly mean number of events during the period (right).

D.2.1 Energy transfer

In his numerical study, Vilibić (2005) used cosine and box air pressure disturbances varying in period/duration, speed and direction as forcing air pressure series to figure out how the Middle Adriatic coastal waters respond to those disturbances. It is documented that larger resonant transfer of energy (from pressure disturbance to sea level) occurs for shorter disturbances and for the box versus cosine variation, in particular in the high-frequency domain. In other words, extreme sea level oscillations occur under short and intense atmospheric disturbances when they match natural frequencies of the corresponding bays/harbours. Oppositely, low-frequency natural modes favour longer atmospheric disturbances, but the energy transfer towards the sea (resonance amplification) may be significantly lower if the shelves are short such as at islands. These results may support the following arguments: (i) the extreme sea level oscillations during Events 15 may be attributed to high frequency atmospheric disturbance, and (ii) low-frequency waves are unlikely amplified at small island sites such as CJ and EC (Here we find the reason of the low sea levels at these sites). These points will be further discussed with the results of numerical experiments.

Hibiya and Kajiura (1982) made a simple estimate of Proudman amplification over a shelf which has limited dimensions and a slowly varying depth. If a speed of an air pressure disturbance is close to a resonant speed, the final height of sea level oscillations $\Delta\zeta$ is given by the following expression:

$$\Delta\zeta = \frac{\Delta\bar{\zeta}}{L_1}\frac{x_f}{2} \tag{29}$$

where $\Delta\bar{\zeta}$ is a sea level change due to the inverse barometric effect, L_1 is a length of the leading pressure increase in its direction of propagation and x_f is a distance travelled by the air pressure disturbance over a shelf (see Figure 18).

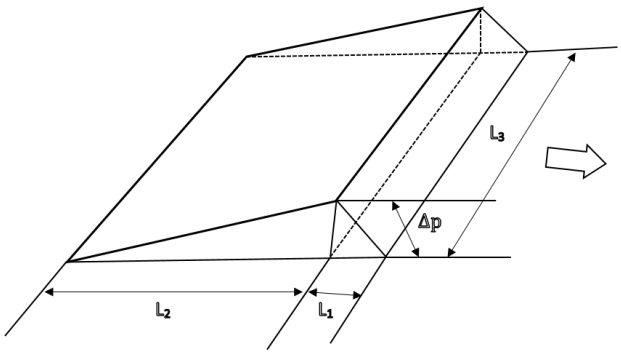

Figure 18: Illustration of an idealized pressure disturbance that Hibiya and Kajiura (1982) used to numerically simulate the monster *Abiki* phenomenon in Nagasaki Bay on 31 March 1979. Here Δp, L_1, L_2 and L_3 represent pressure increase (pressure jump), length of the leading pressure increase, length of the disturbance after the pressure jump and influence range of the pressure jump, respectively (after Hibiya and Kajiura (1982)).

It should be noted that the factors that determine the intensity of a pressure disturbance is L_1 and Δp. L_1 corresponds to the period of the wave that generates the pressure jump (Δp). In addition, amplification by the Proudman resonance is inversely proportional to L_1.
Shown in Table 6 are the amplification factors of sea level due to the Proudman resonance that each event mean pressure jump for its time range (Figure 14) may generate. Here we assume that the disturbance transverses over the Yellow Sea with a constant speed of 26.2 m/s from 299.5^o. These figures show that the dominant periods of an atmospheric disturbance should be short enough, and the travelled distance should be long enough to properly transfer its energy to long ocean waves.

Table 6: The Proudman resonance factor for each mean pressure jump for its time range, with varying travelled distance by air pressure disturbance, assuming that its velocity is constant with a speed of 26.2 m/s and from 299.5^o.

Time range (min)	Pressure jump (hPa)	Length L_1 (km)	Inverse barometric effect (cm)	Proudman resonance factor (expected sea level (cm))		
				x_f = 400 km	x_f = 200 km	x_f = 100 km
128	4.2	201.2	4.2	1.0 (4.2)	0.5 (2.1)	0.3 (1.0)
64	3.6	100.6	4.2	2.0 (8.4)	1.0 (3.6)	0.5 (1.8)
32	3.3	50.3	3.3	4.0 (13.2)	2.0 (6.6)	1.0 (3.3)
16	2.6	25.2	2.6	8.0 (20.8)	4.0 (10.3)	2.0 (5.2)
8	1.9	12.6	1.9	15.9 (30.2)	8.0 (15.1)	4.0 (7.6)
4	1.2	6.3	1.2	31.8 (38.2)	15.9 (19.1)	8.0 (9.5)
2	0.5	3.1	0.5	63.6 (31.8)	31.8 (15.9)	15.9 (8.0)

Now we wish to estimate the event mean L_1. Considering the mean event sea level, 21.5 cm, if we pick just one, the event mean pressure jump time range should be longer than 8 min in case of $x_f = 400km$

(see Table 6). In addition, we need to consider the other resonance effects, including shelf effect and harbour resonance. Thus we may choose 32 min as the tentative estimate because this is in the middle of the two dominant periods (16.5 and 57.6 min) of the event mean disturbances (see Figure 15).
Synthesising the above results, for an mean air pressure disturbance with a 32-min pressure jump of 3.3 hPa and a width L_1 of 50.3 km (here $L_1 = U \times T$, where U is a propagation speed of an air pressure disturbance U, 26.2 m/s, and its period T, 32 min), which propagates for 250 km over the sea of uniform 70 m depths from 299.5^o, the expected mean sea level response for the 49 events due to the Proudman resonance may amount to 8.3 cm. In other word, the inverted barometric effect of 3.3 cm of sea level change by the pressure change of 3.3 hPa may be amplified to 8.3 cm due to the Proudman resonance by a factor of 2.5. Here we set the pressure disturbance speed U to 26.2 m/s, which is the most favourable speed for the Proudman resonance, and we choose the direction of the disturbance, 299.5^o, which is the median between the total median (277.5^o) and the NW group median (321.5^o) (see Figure 16). This is because the member of the NW group outnumbers the SW group by 2, and if we take the total median (277.5^o), which may be one of the most favourable directions for the Proudman resonance and shelf effect, model will over estimate.

D.3 Numerical Experiments

Two numerical experiments were conducted to simulate an estimated mean event long ocean wave propagation, and the disastrous event of 31 March 2007 (Event 15).
We used the 2-D non-linear shallow-water model that Vilibić et al. (2008) used to simulate the destructive meteotsunami of 15 June 2006 on the coast of the Balearic Islands (see Section B.7). The model domains are set as in Figure 19 and Table 7.

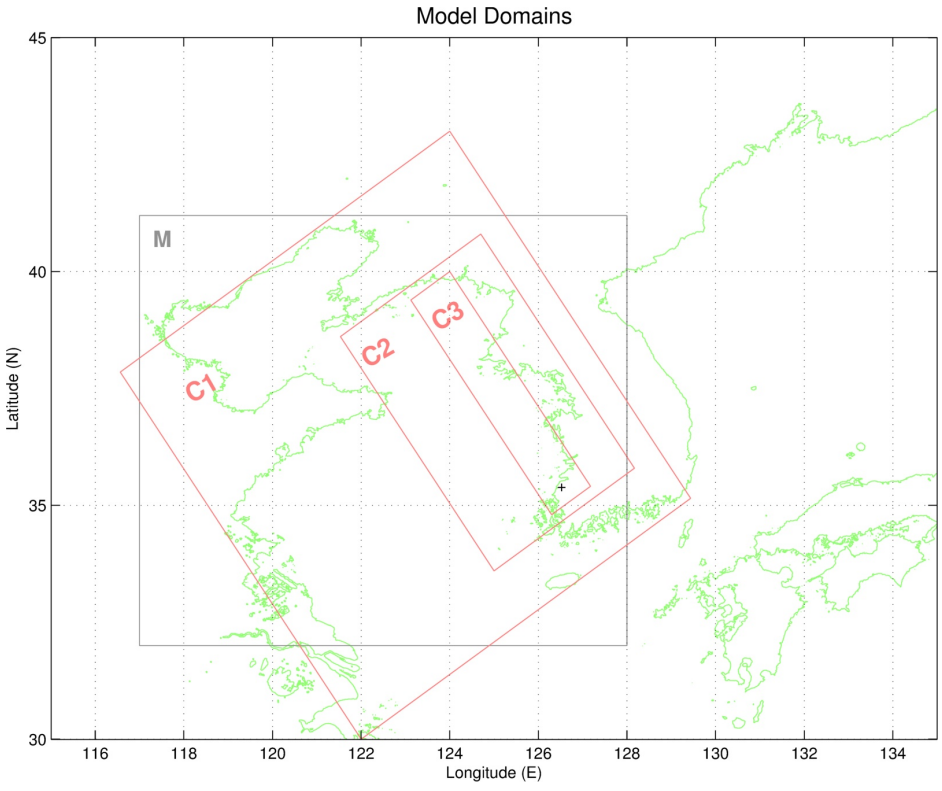

Figure 19: Model domains.

Table 7: Model domains

Experiment No.	Domain name	Grid cells	Grid distance (km)
I	M	185×221	4.7×5.5
II	C1	127×254	4.7×5.5
	C2	155×245	2.3×2.8
	C3	130×673	0.76×0.92

We used the GEBCO 30 arc-second bathymetry grid data for sea depths. Time steps were taken to be $dt = 15s$ according to the GFL condition, $\sqrt{gh_{max}}\Delta t \leq \frac{\Delta}{\sqrt{2}}$. The bottom roughness scale z_0 was set to be 0.001 m. The sea was supposed to be at rest at $t = 0$, and the coast is a rigid wall. The radiation condition was used at all the open boundaries of M and C1 (Raymond and Kuo, 1984). Each host model provides boundary values to the nested models. The flow relaxation scheme were applied to the boundary zones of C2 and C3 (Jones et al., 1995).

Numerical Experiment I

The first experiment aims to simulate the propagation of an event mean long ocean waves in terms of the Proudman resonance and shelf effect based on the estimated scales of the mean atmospheric disturbances in the previous section. We used the method that Hibiya and Kajiura (1982) applied to create forcing pressure fields for a simulation of the monster meteotsunami at Nagasaki Bay in 1979.
Since we are focusing on the Proudman resonance and shelf effect, we selected three different time ranges of 16, 32 and 64 min, which are most dominant periods of the atmospheric disturbances during the events. We made a forcing pressure time series, by averaging the three time series, based on the scheme by Hibiya and Kajiura (1982) as shown in Figure 20. The averaged time series and its wavelet power spectra are presented in Figure 21. Here we set L_2 to 3 times of L_1. We set the length of the disturbance to 300 km, which covers all the event sites. We interpolated this series into all the grids within the influence boundary, assuming that the disturbance is approaching from 299.5^o at a constant speed of 26.2 m/s (Figure 22).

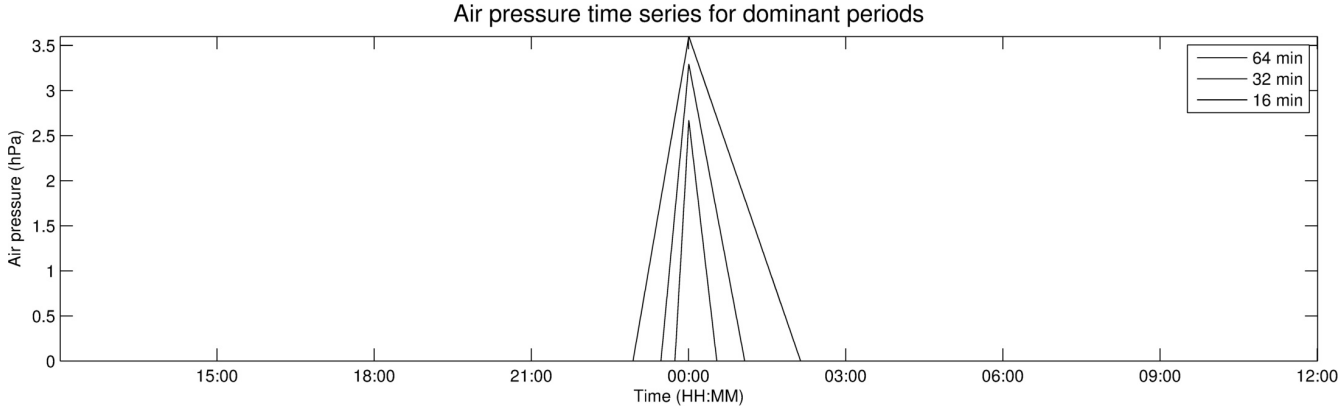

Figure 20: Illustration for making forcing pressure time series using the scheme by Hibiya and Kajiura (1982). The forcing pressure series is the mean of these series.

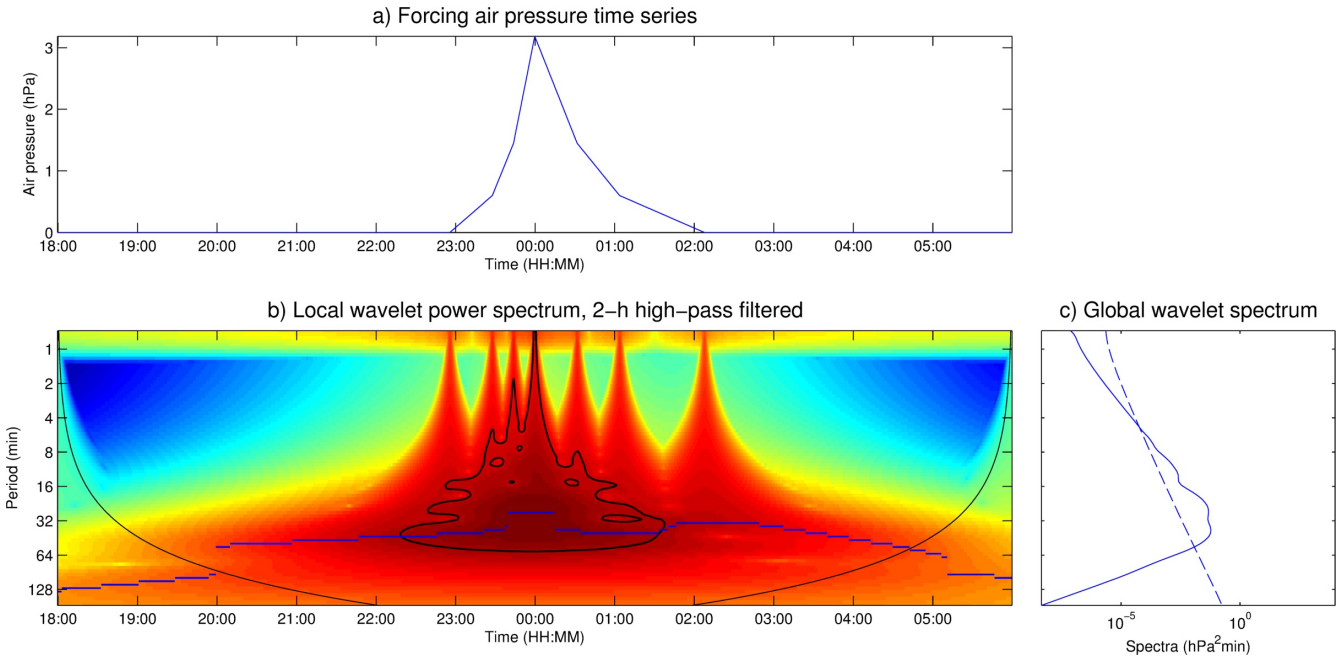

Figure 21: Forcing pressure time series (a), and its wavelet power spectra (b and c).

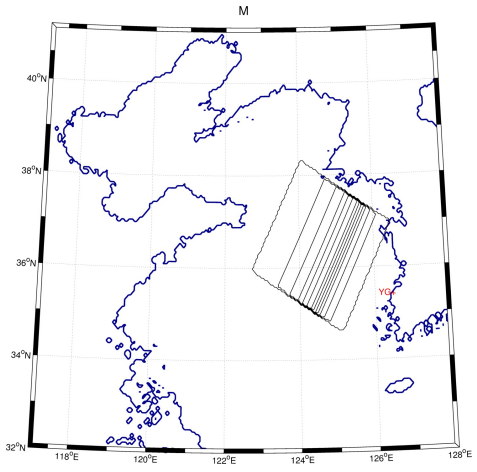

Figure 22: Illustration of the forcing pressure field. Contours are drawn with increments of 0.5 hPa.

Here we present two simulated fields of sea level in Figure 23. The left chart depicts the sea levels traced by the crest of the atmospheric disturbance. The thick black line indicates the lowered sea level of -3.2 cm by the increased air pressure of 3.2 hPa. We may consider that the Proudman resonance occurs in the area surrounded by the line. From this, we can see that the Proudman resonance occurs over the sea area with depth of 60-80 m. When the propagating waves encounter slopes, they starts rising until the slops become slow. We may regard the area enclosed by the -3.2 cm contour line and the imaginary line connecting the local maxima as the shelf effect zone, and beyond the line to the coastline as the seiche zone. The right chart is the modelled absolute maximum sea level field. We can see heightened waves at bays, seiches, which are made by the following waves. It is noted that waves along the coast between GS

and AH are the most excited. It may be related with the fact that this area is the saddle point between the two peaks indicated by A and B (left chart).

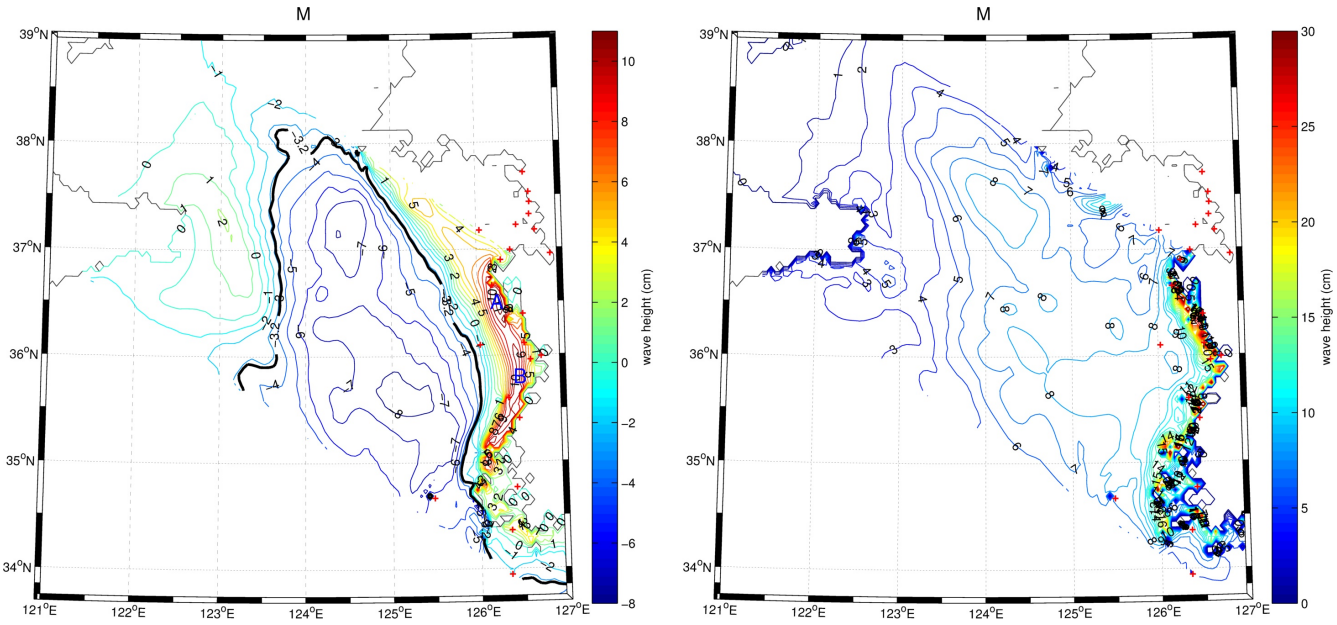

Figure 23: Results of model run for the simulation of long ocean waves induced by the estimated event mean atmospheric disturbance.

The estimated resonance factors for each event site are summarised in Table 8 based on the intervals for the Proudman resonance, shelf effect and harbour oscillations (seiches) explained above, and the vertical sections (to the direction of 299.5^o) of the model outputs (see Figures 24 and 25 for YG and HS for reference, the results for the other event sites are attached to Appendix). Here the harbour resonance factors are based on the observed sea levels because the model does not forecast inside harbour resonance. The figures explain that the Proudman resonance and harbour resonance do more important roles than shelf effect. Although the resonance factors vary in velocity of air pressure disturbance and its dominance periods, the estimated Proudman and shelf resonance factors may be good approximates to characterise normal meteotsunami in the Yellow Sea in particular for one from the north-west. However there exists a certain amount of uncertainty in the harbour resonance factors, which are highly depends on natural periods and shape of coastlines.

Table 8: Estimated amplification factors based on the model results.

Site	YG	MP	GS	CJ	JH	BR	WD	AH	HS	EC	Mean
Inv. barometric effect (cm)	3.2	3.2	3.2	3.2	3.2	3.2	3.2	3.2	3.2	3.2	3.2
Fetch, x_f, (km)	330	290	240	370	265	110	330	100	240	285	255
Proudman resonance (cm)	9.0	9.7	7.2	4.5	7.0	6.5	8.5	6.1	8.0	7.2	7.4
(Amplification factor)	(2.8)	(3.0)	(2.3)	(1.4)	(2.2)	(2.0)	(2.7)	(1.9)	(2.5)	(2.3)	(2.3)
Shelf effect (cm)	14.0	12.5	12.5	5.0	14.0	3.3	11.9	11.2	8.0	7.3	10.0
(Amplification factor)	(1.6)	(1.3)	(1.7)	(1.1)	(2.0)	(0.5)	(1.4)	(1.8)	(1.0)	(1.0)	(1.3)
Observation (cm)	31.6	18	23	15.4	30.7	9.8	23.5	28.8	20.7	13.8	21.5
(Harbour res. amp. factor)	(2.3)	(1.4)	(1.8)	(3.1)	(2.2)	(3.0)	(2.0)	(2.6)	(2.6)	(1.9)	(2.3)

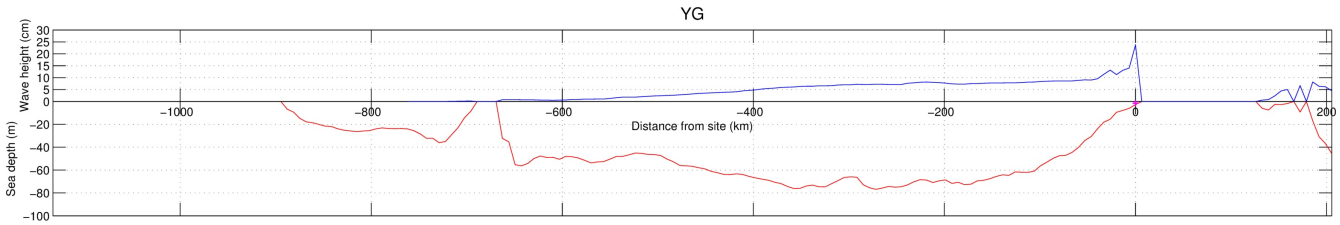

Figure 24: Simulated event mean propagation of long ocean waves for YG.

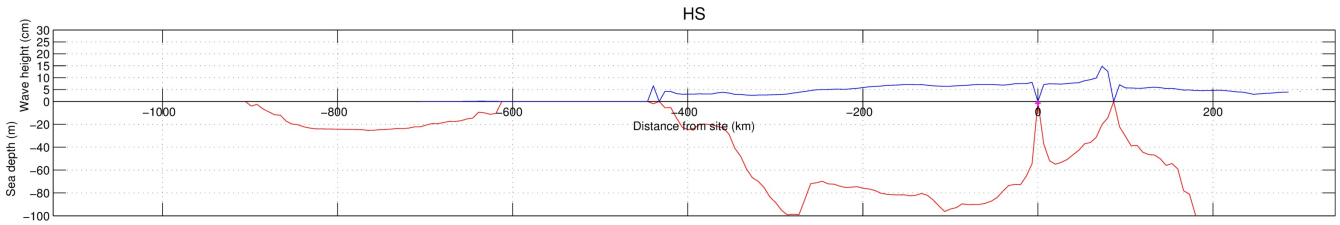

Figure 25: Same with Figure 24 but for HS.

Experiment II

We implemented another numerical experiment in regard to Event 15, which was the most significant. Figures 26 and 27 show the MSLP time series and their wavelet power spectra, which generated vigorous sea level oscillations to the west coast. The series are featured by a relatively long duration (about 9 h), with two different disturbance types (refer to Figures 13 and 27). The Locations and times of the first outstanding pressure jump of these series are indicated in Figure 28.

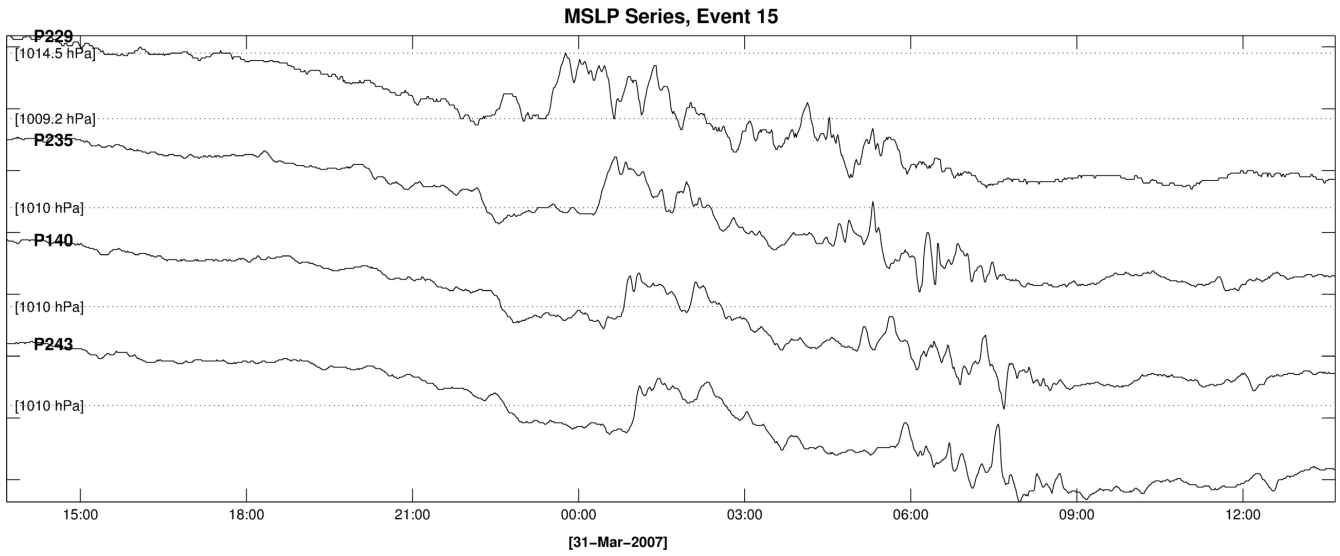

Figure 26: MSLP series at some sites during Event 15 (see Figure 28 for their locations).

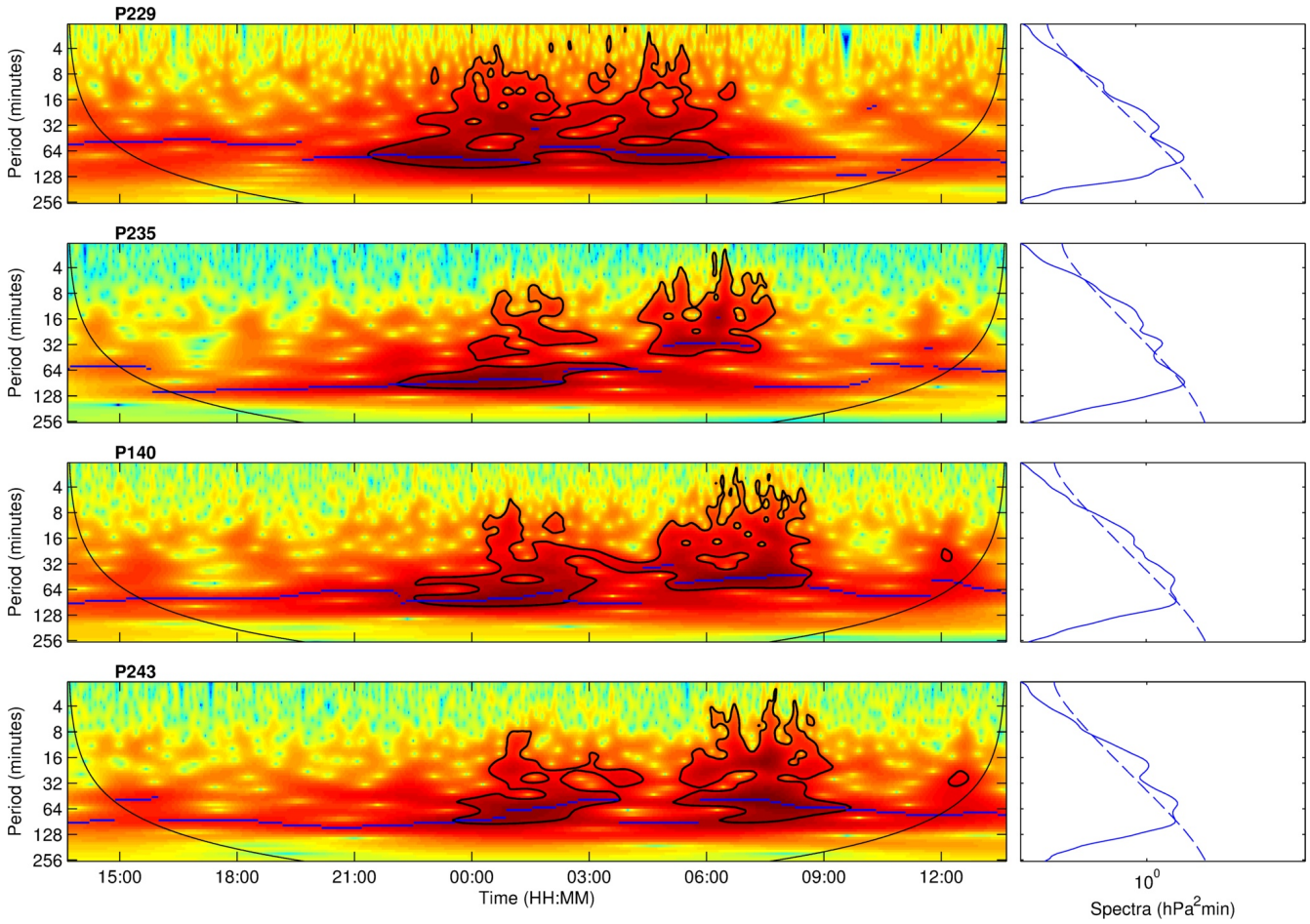

Figure 27: 2-h high-pass filtered wavelet power spectra for the series above.

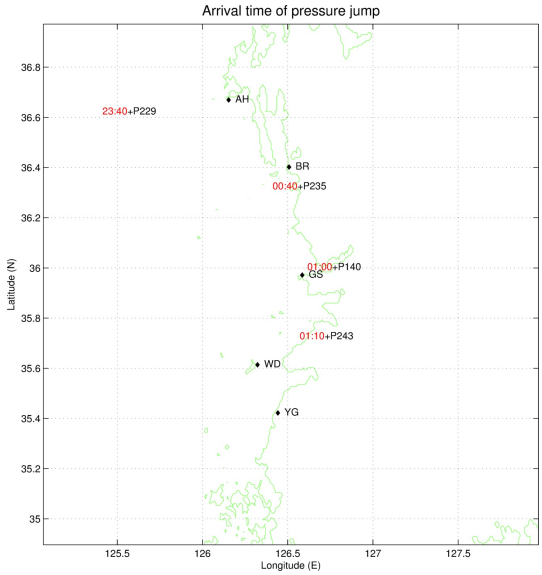

Figure 28: Locations of MSLP and sea level sites and pressure jump arrival times (in red) (after KMA (2013)).

We referred to the two former studies on estimating the velocity of the atmospheric disturbance related with the event (KMA (2013) and Eom et al. (2012)), and set the disturbance speed to 24.5 m/s and direction from 325.3^o. Assuming that the velocity is not changing, we shifted in time the MSLP series at the first site, P229, to YG to set the peak time of the disturbance to match the maximum sea level oscillation ($24.5m/s \times 112min = 164km$), and interpolated it into all the grid points (It turns out that disturbances occurred in a larger area, covering all the sea level sites.). Thus the forcing field targets at the two sites with the highest amplitudes of sea level, WD (131.3 m) and YG (131.7 m) (the MSLP site P229, WD and YG are almost in the same line of the propagating disturbance). Figure 29 shows the forcing MSLP field at a certain time.

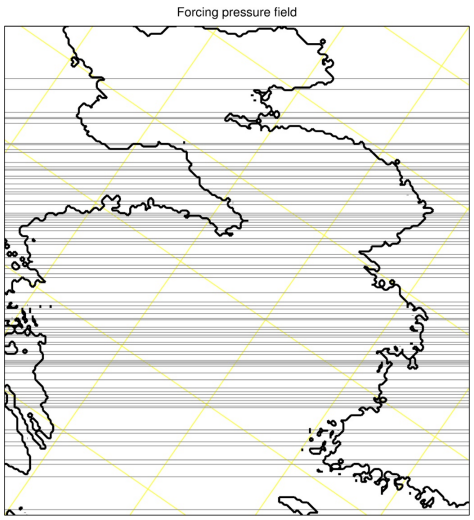

Figure 29: Forcing pressure field. Contours are drawn in increments of 1 hPa.

Figure 30 shows the modelled composite maximum sea level field, after 2-h high-pass filtering, by C, It shows that the disturbance with pressure jump of 6.3 hPa for 64 min amplified waves to WD and YG up to about 30-40 cm due to the Proudman resonance and shelf effect by factor of 4.8-6.3. Again, it should be noted that the air pressure forcing targets at the two sites, so waves at other regions can be far from the truth as distance becomes far from the sites. Nevertheless, the figure depicts the effect of the Proudman resonance and shelf effect over the sea.

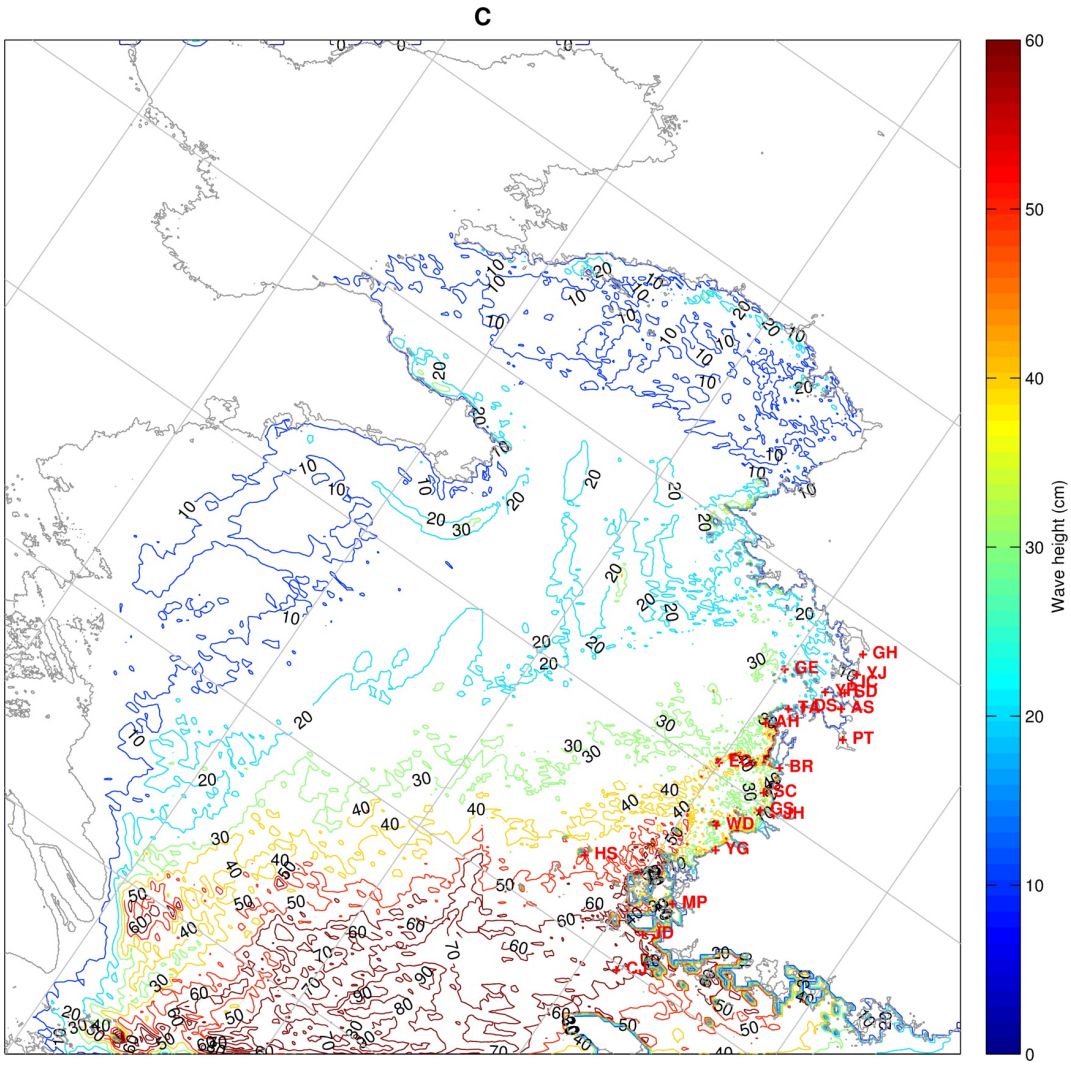

Figure 30: Composite field of modelled maximum sea level after 2-h high-pass filtering.

Figure 31 shows modelled sea level series (red) by C3 and observations after a 2-h high-pass filtering. The main feature is that the model does not simulate the peak oscillations. The main reason is that the model is not able to simulate inside harbour oscillations because the resolutions are too coarse. The worse results for AH, BR, and GS are due to the fact that the forcing signal has been chosen to target at the two sites, WD and YG. From the model results, we can say that the estimated direction and speed of the disturbance is quite accurate. However simulations using high resolution models should be necessary for details.

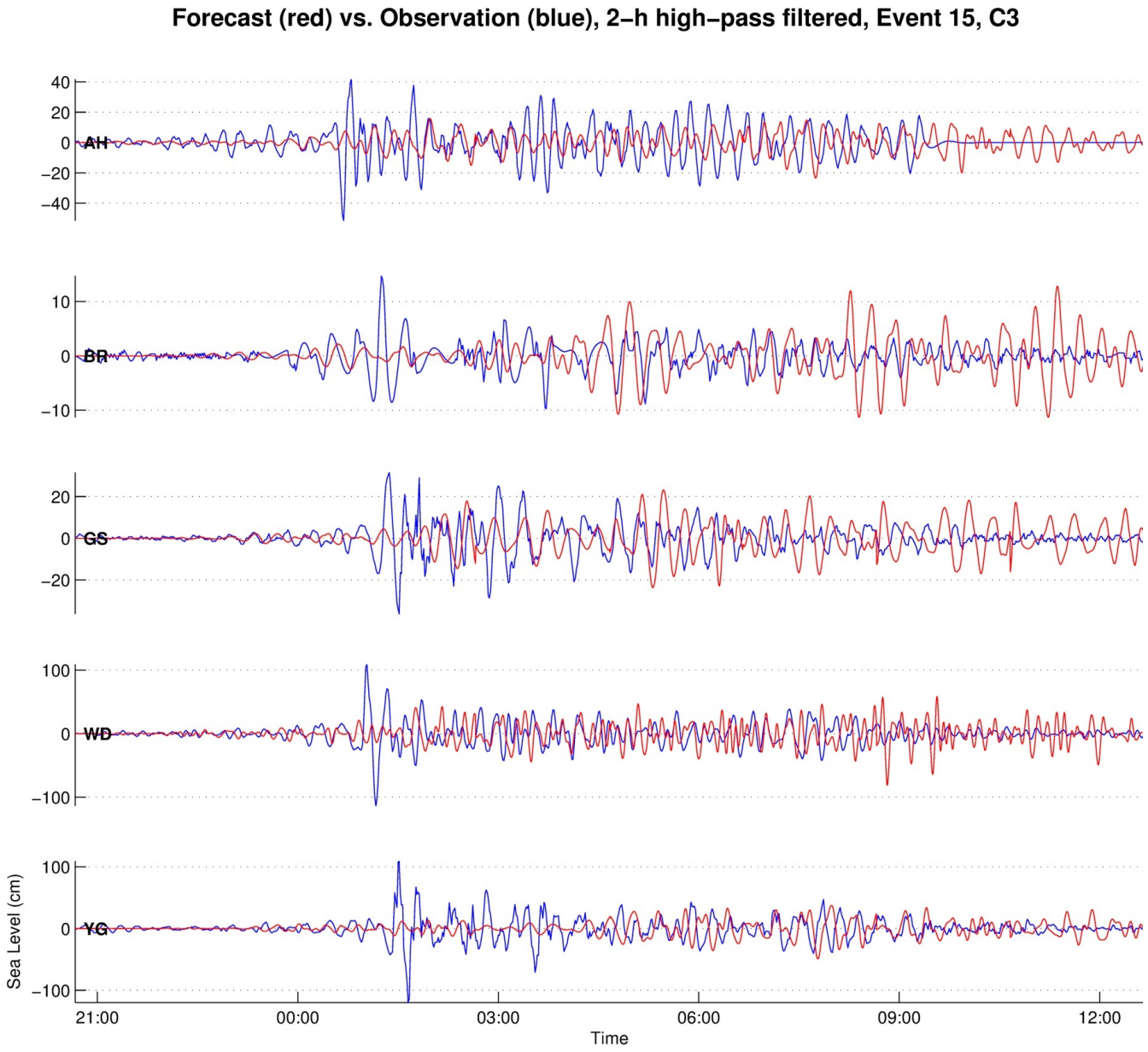

Figure 31: Comparison of time series between observations (blue) and forecasts (red) by C: time series after 2-h high-pass filtering.

Compared with the forcing pressure signal, one important feature of the sea level observation series is that inside harbour resonance occurred only by the first disturbance but not by the second disturbance, i.e., energies were transferred less by the second disturbance at high frequencies. Figure 32 is comparison between the MSLP and sea level time series and their wavelet spectra of the two sites close to each other (see Figure 28). Although the second disturbance (during about 04:00-08:00) is more vigorous than the first one (during about 22:00-04:00) at high frequencies, more energy was transferred by the first disturbance to the ocean waves in particular at high frequencies (periods of 2-8 min). Such characteristics are related with the shape of atmospheric disturbance.

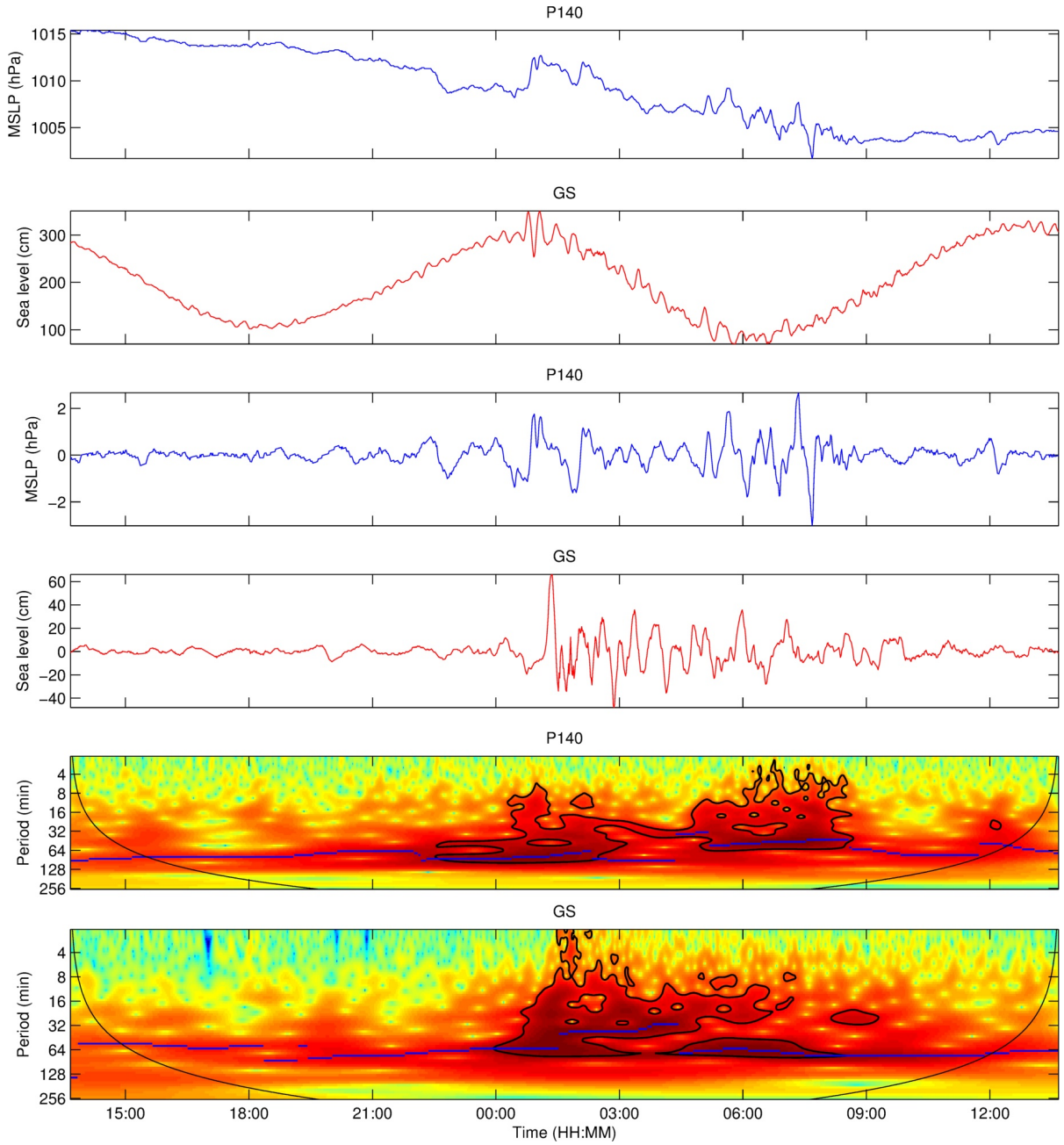

Figure 32: Comparison of MSLP and sea level time series (the 1st and 2nd panels), their 2-h high-pass filtered time series (the 3rd and 4th panels, and their wavelet power spectra (the 5th and 6th panels).

Figure 33 presents the time series and its wavelet power spectra of P229, which is considered to have directly affected the sea level oscillations at WD and YG. The pressure jumps at the second disturbance are much higher than at the first disturbance. However the pressure jump maxima for all the time ranges at the first disturbance takes place at the same time, whereas the high pressure changes at short time ranges are not in line with the longer range pressure jumps at the second disturbance. These explain that box-type disturbance transfers energy to ocean waves in a more efficient way. This is due to the spectral characteristics of a box disturbance that energy decreases as going towards higher frequencies at a significantly lower rate than cosine disturbance (Vilibić, 2005).

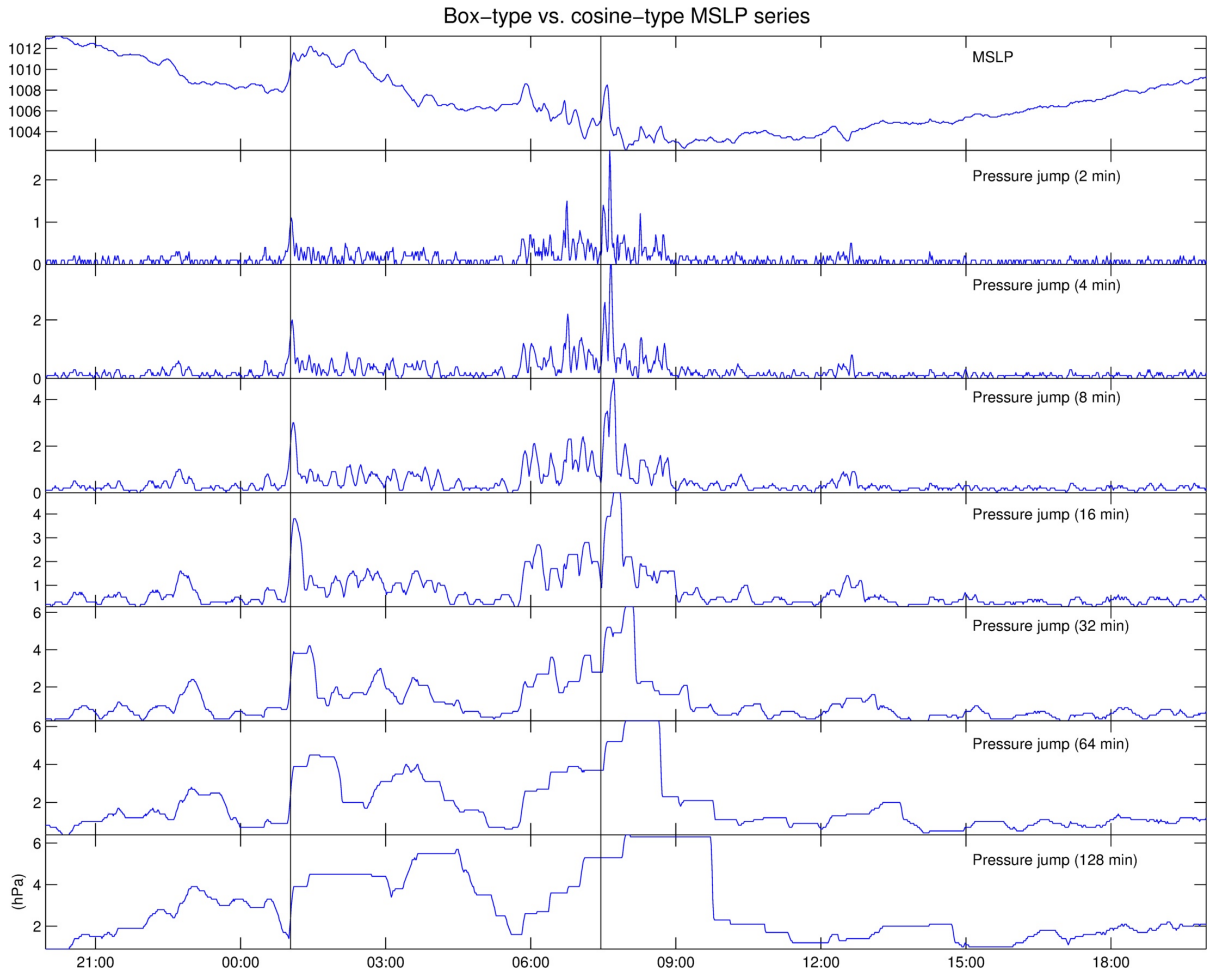

Figure 33: Comparison of pressure jumps between at the box-type and at the cosince-type disturbances of P229.

Summing up, the record-high sea level oscillations at WD and YG are blamed by high-frequency (periods of 2-8 min) waves of 20-30 m, which were generated by an intense box-type disturbance, featured by a sharp increase of pressure, 1.2, 2, 3, and 3.7 hPa for 2, 4, 8 and 16 min, respectively. The incoming ocean waves were amplified due to harbour resonance up to 131.7 cm at YG an 131.3 cm at WD by a factor of 4.3-6.5.

E Discussion

Synoptic setting

It is considered that at the saddle point of the four major systems with different characteristics, the atmosphere over the Yellow Sea can be easily influenced by them, and things happen as the jet steak develops from the north-west, which is associated with a large differential in temperature between the north and the south at the lower levels as the maritime tropical air mass expands. This plays a pivotal role in forming cyclonic circulation centred over the Manchuria region and surface lows around 35N. The positive vorticity max over Manchura spawns surface lows, which is regarded as one of the most prominent features of the typical synoptic setting favourable for meteostunamis in the Yellow Sea in spring. This

argument is supported by the fact that among 49 events, 22 events occurred in couple in a row for two days (Events 8-9, 10-11, 14-15, 20-21, 24-25, 26-27, 28-29, 31-32, 37-38, 41-42 and 43-44).
The two patterns of atmospheric disturbance movement, approaching from the north-west and from the south-west, occur corresponding to the evolution of the typical synoptic setting. Figure 34 shows the group means of MSLP, 500 hPa relative vorticity and 300 hPa wind speed of the two patterns, which were produced from the reanalysis data based on the estimated disturbance velocities in the previous section (refer to Table 5 and Figure 16). One of the most important features in common between the two groups is jet stream shear at the level of 300 hPa. Jet stream shear is related with atmospheric disturbance producing gravity waves (Pavelin and Whiteway, 2002), which are also associated with meteotsunami (Šepić et al. (2009) and Monserrat et al. (1991)). The jet streak shape of the NW group (a3) represents the peak stage of the typical synoptic setting. However the one for the SW group depicts early or late stage of the typical setting. In addition, the position of each jet streak shear explains the different direction of atmospheric disturbance. The reason of higher speed of the atmospheric disturbances of the SW group (45.6 m/s vs. 20.4 m/s) is due to the fact that winds at the downstream jet streak sector are much faster than at the upstream jet streak sector (refer to the 300 hPa event mean wind chart).

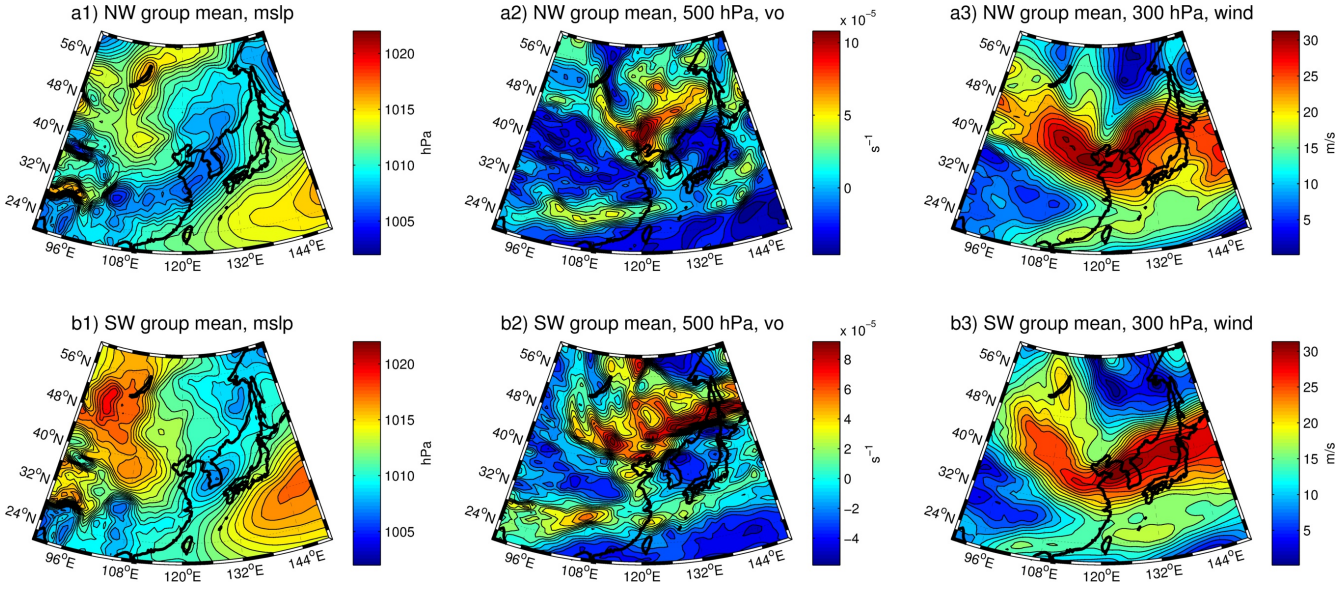

Figure 34: Mean MSLP, 500 hPa relative vorticity and 300 hPa wind speed charts of the NW group and SW group of atmospheric disturbance.

Figure 35 are normalized event means of 300 hPa wind speed and 500 hPa geopotential, which depicts the evolving event mean jet stream and trough during the typical synoptic setting for 24 hours. The normalized jet streak core passes North Korea, developing the trough at the level of 500 hPa for 24 hours, during which a couple of meteotsunamis can possibly occur in a row.

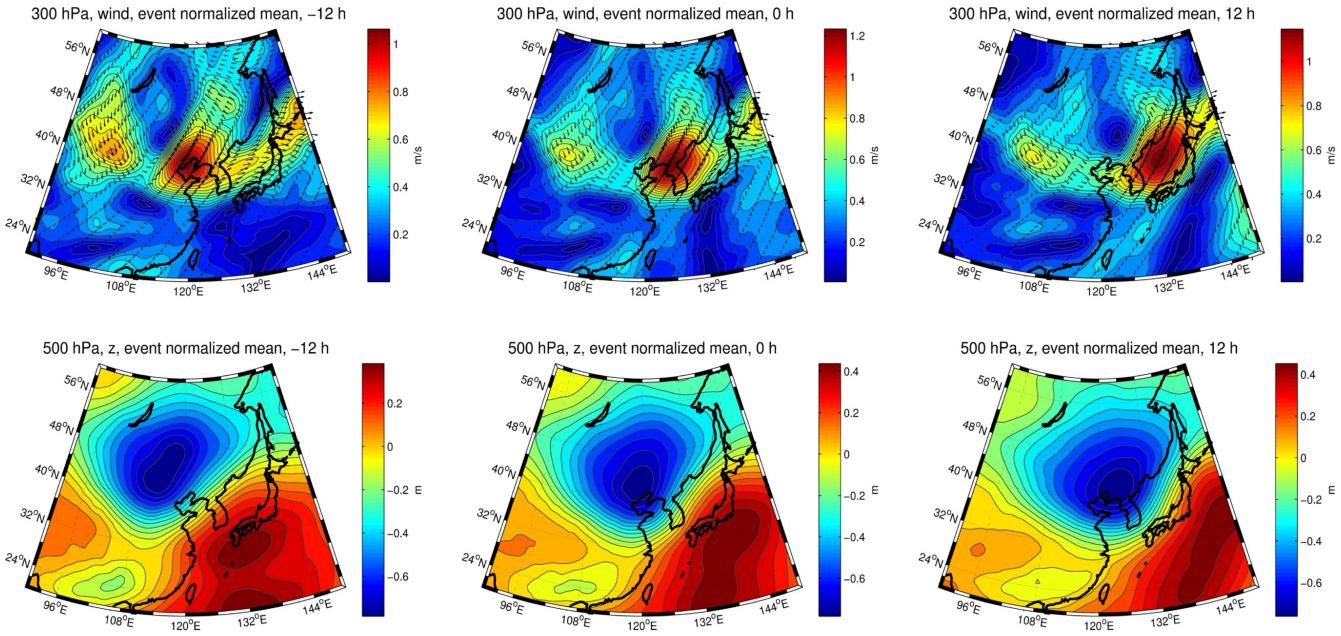

Figure 35: Normalized event means of 300 hPa wind (upper panels) and 500 hPa geopotential (lower panels) 12-h before (left panels), 12-h after (right panels) and at the peak time (center panels) of the meteotsunami events.

Interpretation of EOFs

Based on the above results, we find that the 500 hPa relative vorticity EOFs 1 and 2 may best match the two types of direction (Figure 36). The positive vorticity max over Bohai Bay (EOF 2) may develop surface lows approaching from the south-west, whereas the vorticity max over the North-East China is more related with the development of surface lows coming from the north-west. Regarding the MSLP EOFs presented in Section D.1, we conclude that the first EOF, which explains 43.4 % of the total variance, is more related with the early or late typical synoptic setting. The second EOF, which accounts for 13.7 % of the total variance, is considered to represent a developed surface low at the mature stage of the typical synoptic setting.

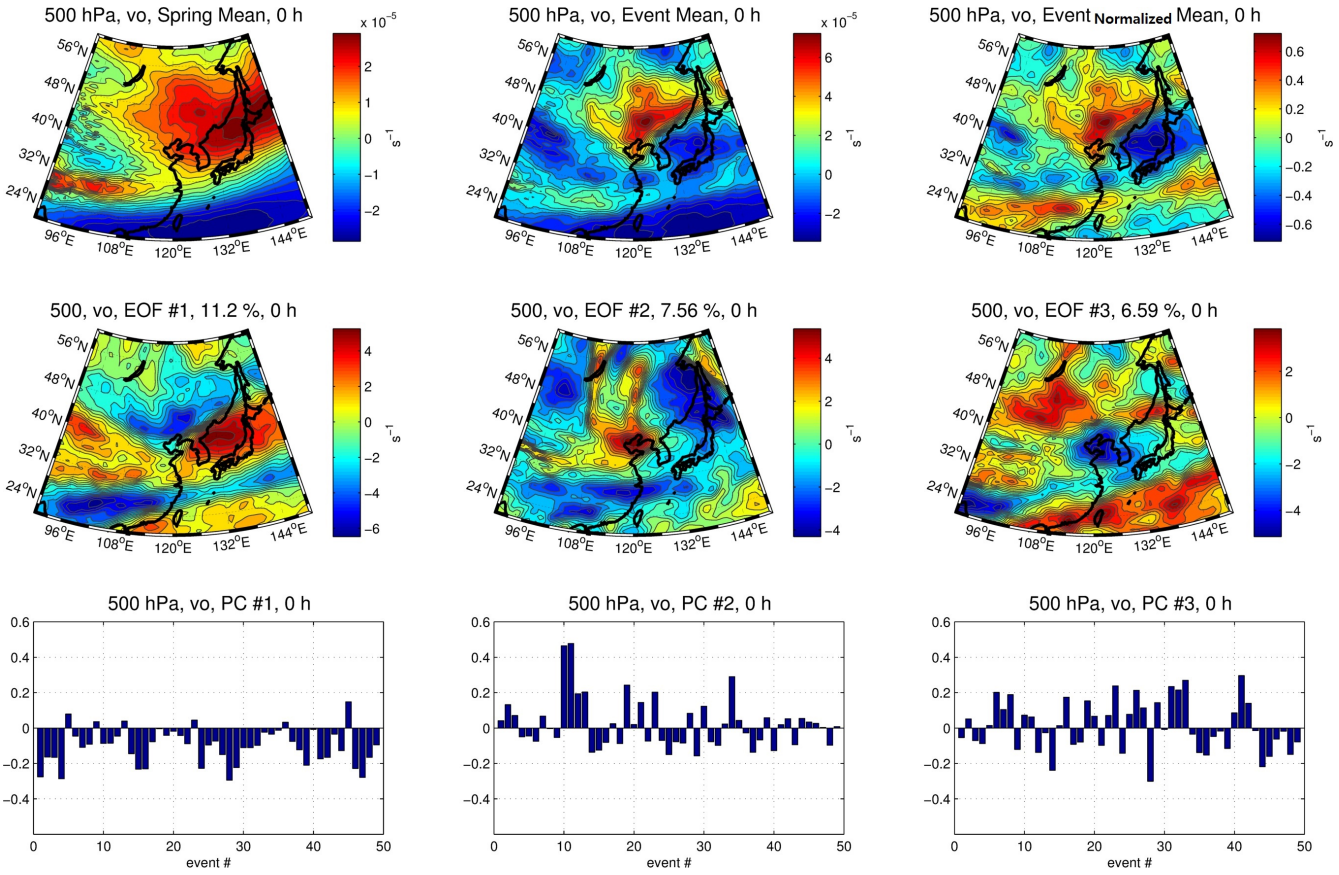

Figure 36: Same with Figure 9 but for the 500 hPa relative vorticity.

The surface pressure EOFs are in line with those of the 500 hPa geopotential and the 300 hPa wind, which also characterise the developing typical setting (Figures 37 and 38). The EOF 2 of the 500 hPa geopotential, which explains 16.2 % of the total variance, depicts the developed trough from the northwest, which is considered as the mature stage of the typical setting. The EOF 1 (with 46.8 %) may explain the possibilities of influences by both the trough centred around Mongolia (NW pattern) and the cut-off trough over the South China (SW pattern). The first EOF of the 300 hPa wind, which accounts for 27.3 % of the total variance, depicts the high speed of wind over the Manchuria area at the matured stage of the typical setting, and the second EOF (with 17.1 %) explains the increasing speed of the northern jet streak over around Mongolia at the early stage of the typical setting.

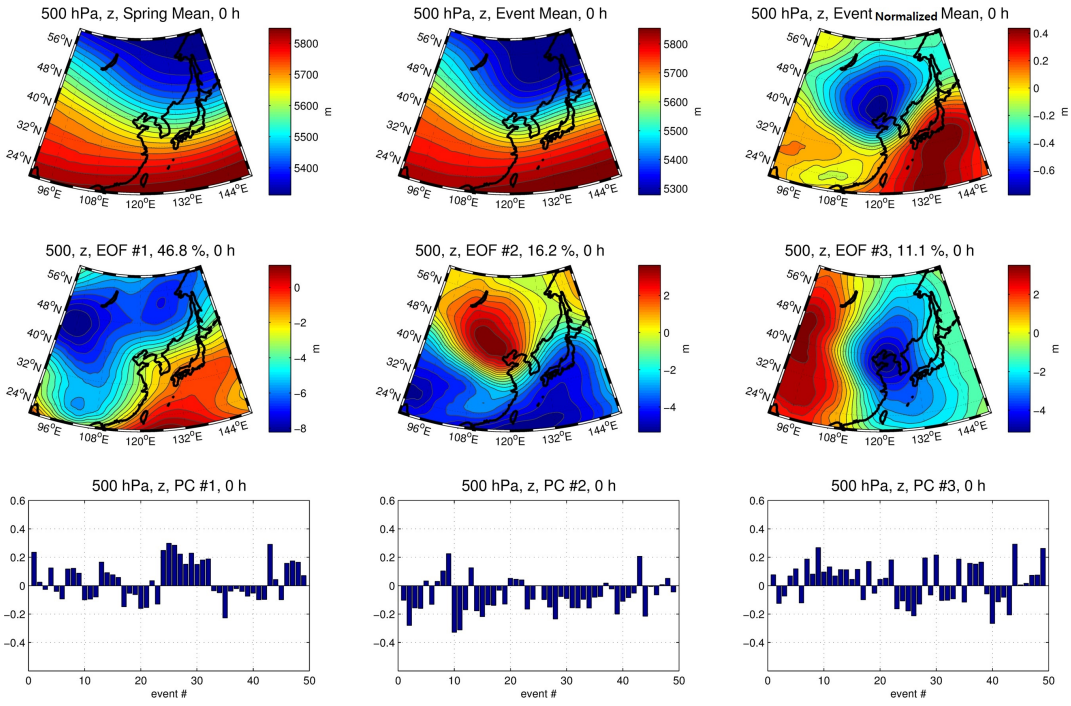

Figure 37: Same as 9 but for the 500 hPa geopotential.

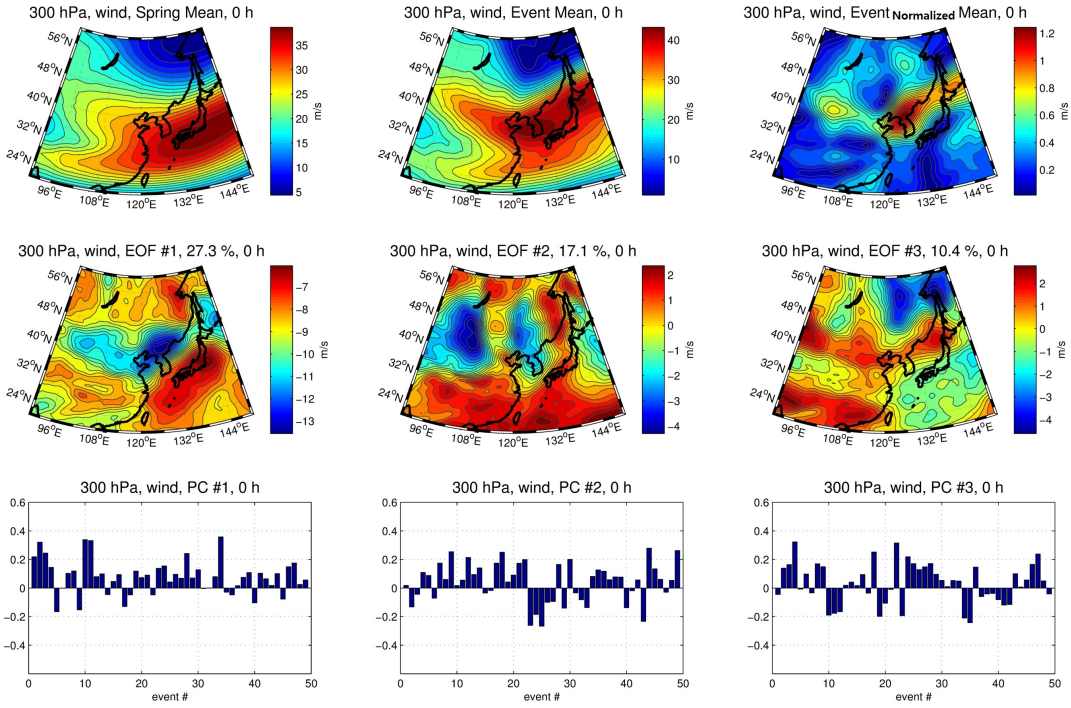

Figure 38: Same as 9 but for the 300 hPa wind.

Estimation of atmospheric disturbance velocity

The Froude number, F_r, may play more important roles than atmospheric disturbance intensity in inducing meteotsunami because an atmospheric disturbance with a strong pressure change more than 4 hPa moves as fast as 60 m/s over a shallow water with depth of 40 m ($F_r \approx 3$), may loose resonance effect. Thus accurate forecasting of generation and velocity of atmospheric disturbance is very important for operational forecasting and warning of meteotsunami. It was found by a number of studies that wind velocity at the level of 500 hPa often matches the speed and direction of atmospheric disturbances during meteotsunami events (Šepić et al., 2012). Thus we retrieved upper-air wind velocity values over the Yellow Sea from the ERA-Interim reanalysis fields for the 14 atmospheric disturbance events shown in section D.2. It reveals that in speed the wind speed at the level of 700 hPa is closer than at the level of 500 hPa to the estimated pressure disturbance speed, but in direction the level of 500 hPa a little more approximates the estimates.

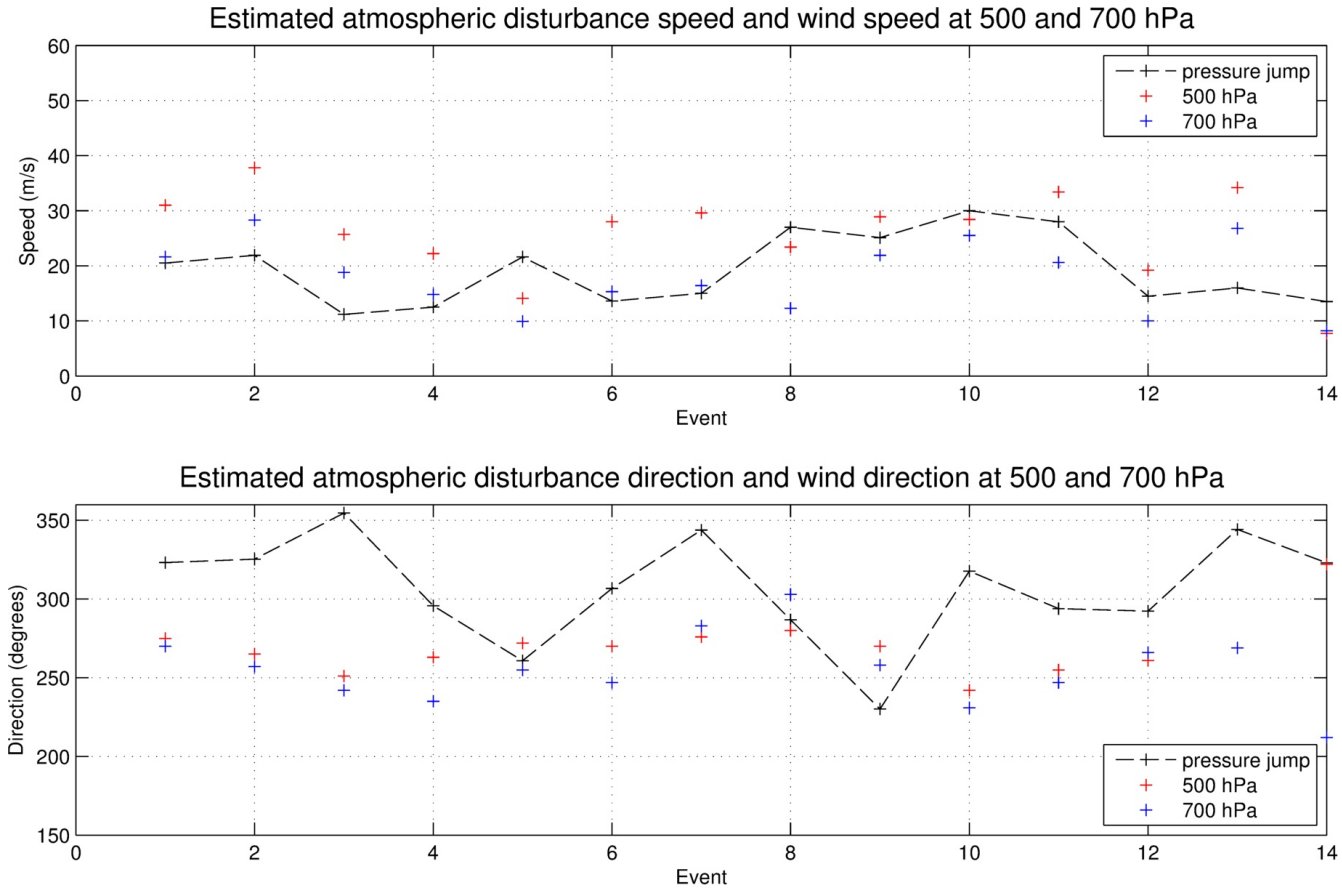

Figure 39: Estimated velocities of the atmospheric disturbances based on the movement of pressure jumps in spring during 2006-2014 (KMA, 2013) and wind velocities of 500 and 700 hPa at the arrival times of the pressure jumps.

Speculation about Event 19

As discussed in the previous section, the meteotsunami of 31 March 2007 (Event 15) is featured by high-frequency sea waves coupled with very intense atmospheric disturbances. Based on the previous results, we conjectured about possible reasons of another damage-caused event, Event 19.

The meteotsunami on 4 May 2008 (Event 19), which caused devastating loss of lives and properties, is

considered a very exceptional phenomena because nearby sea level gauges recorded low sea level oscillations (6.2 cm at BR and 7.6 cm at GS). Figure 40 presents estimated direction of the long ocean waves estimated from the event sites by the KMA (KMA (2013)), and locations of the accidents: Jukdo (indicated by JD) with heavy casualties, and Gaeyado (indicated by GS), which is in front of GS, with property damages. The sea levels with the significant level, 14.8 cm at HS, 9.9 cm at EC, 19.7 cm at WD and 18.4 cm at YG (see Table 3), indicate that waves were decayed at GS and BR. The low sea level at BR (6.2 cm) may be due to decayed energies by the surrounding islands.

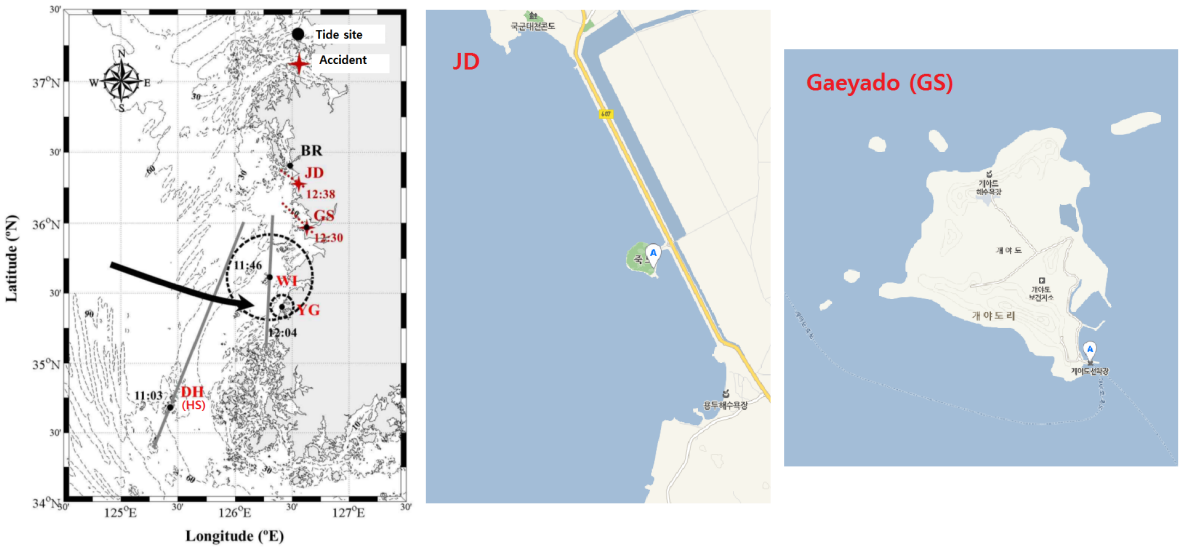

Figure 40: Estimated propagation of long ocean waves and locations of accidents and tide sites for Event 19 (after KMA (2013)). The horizontal lengths of the islands indicated in the pictures are about 400 m and 1.6 km respectively.

Figures 41 and 42 are 4-h high-pass filtered time series of MSLP at P140 and sea level at GS, which are adjacent to each other (refer to Figure 28 for their locations). Here we can see that unlike WD and YG, who have various natural periods (refer to Table 4), waves are excited only at the periods close to the natural period of GS (12.5 min) by a broad band pressure forcing. From this point we can speculate that the damage at the island is related with harbour resonance of waves with amplitude of about 10 cm at the periods ranging 2-8 min.

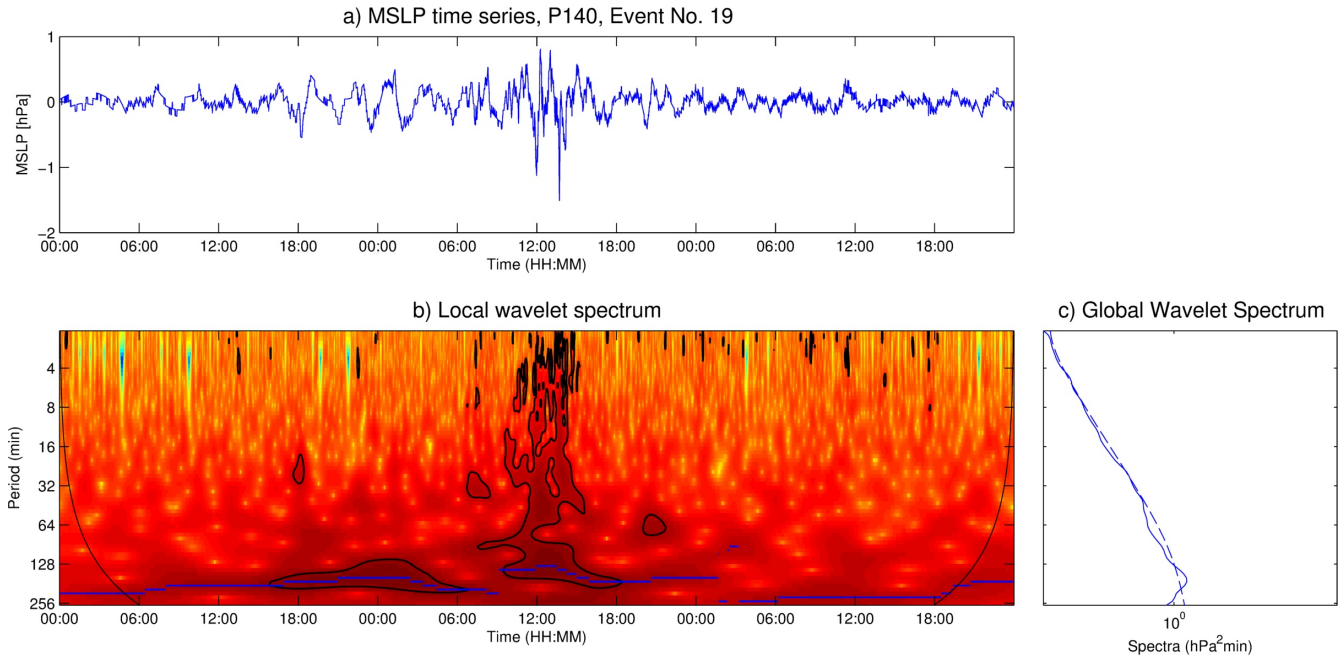

Figure 41: MSLP time series after 4-h high-pass filtering and its wavelet power spectra at P235.

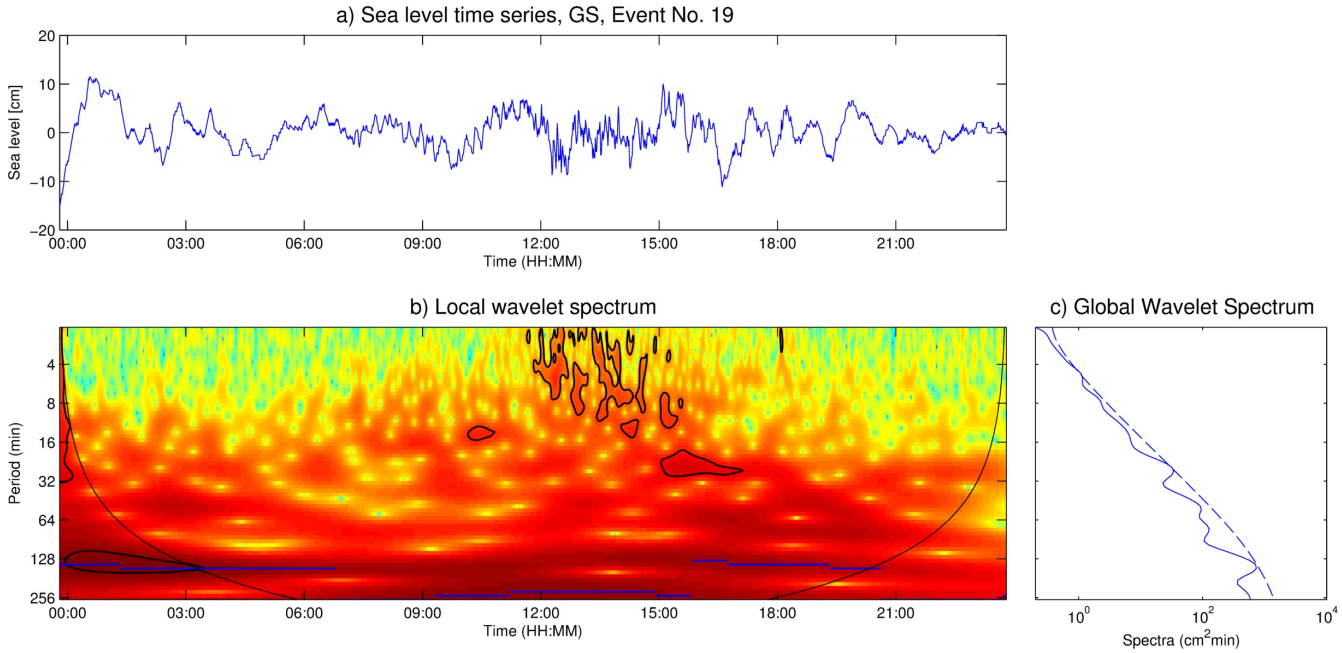

Figure 42: Sea level time series after 4-h high-pass filtering and its wavelet power spectra at BR.

Regarding the other spot, JD, Figures 43 and 44 are the same but for P235 and BR, which are close to each other (refer to Figure 28). The atmospheric disturbance global wavelet spectrum shows peaks at the periods of 5.5 and 26.9. Also, the sea level global wavelet power spectrum have peaks at the periods of 4.7, 20.3 and 63.0 min, which are similar to each other. Unlike BR, the accident place is open to the sea. In particular, as shown in the previous section the place is where incoming long ocean waves converge (see Figure 23). Thus we guess that the incoming long ocean waves were as high as at WD and YG, around 20 cm or more, and that the seiche waves due the the incoming ocean waves may be the reason for the accidents. We will conduct further research on this event in detail in the future.

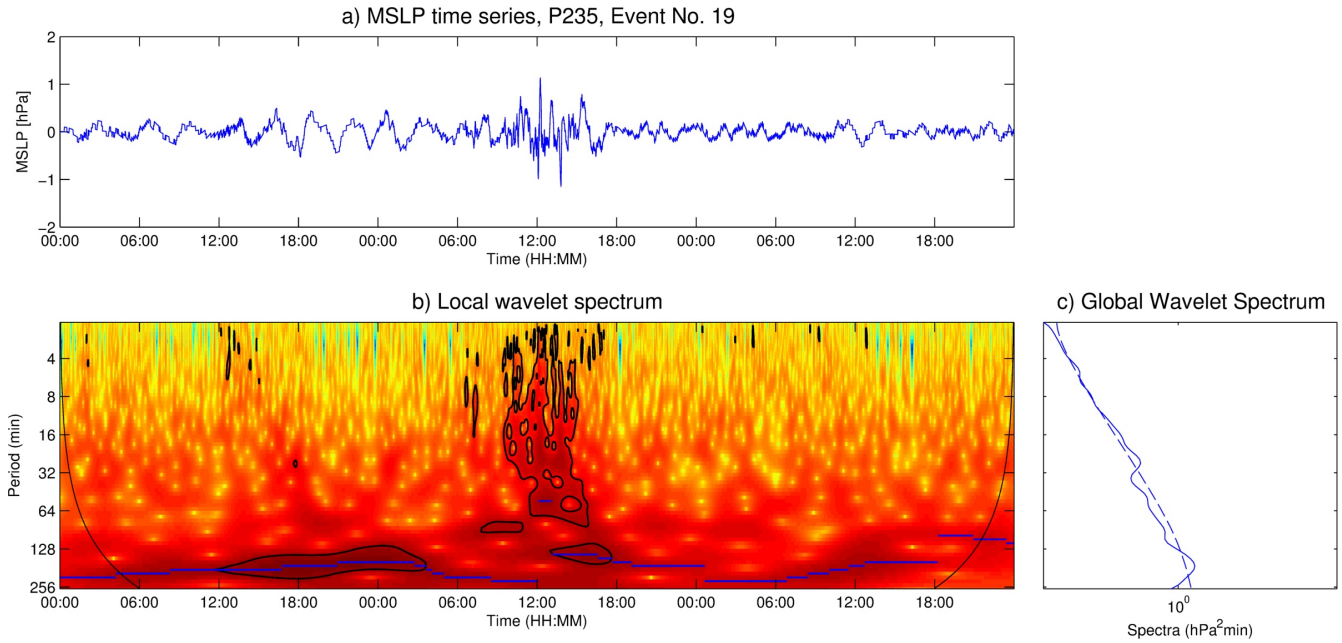

Figure 43: MSLP time series after 4-h high-pass filtering and its wavelet power spectra at P235.

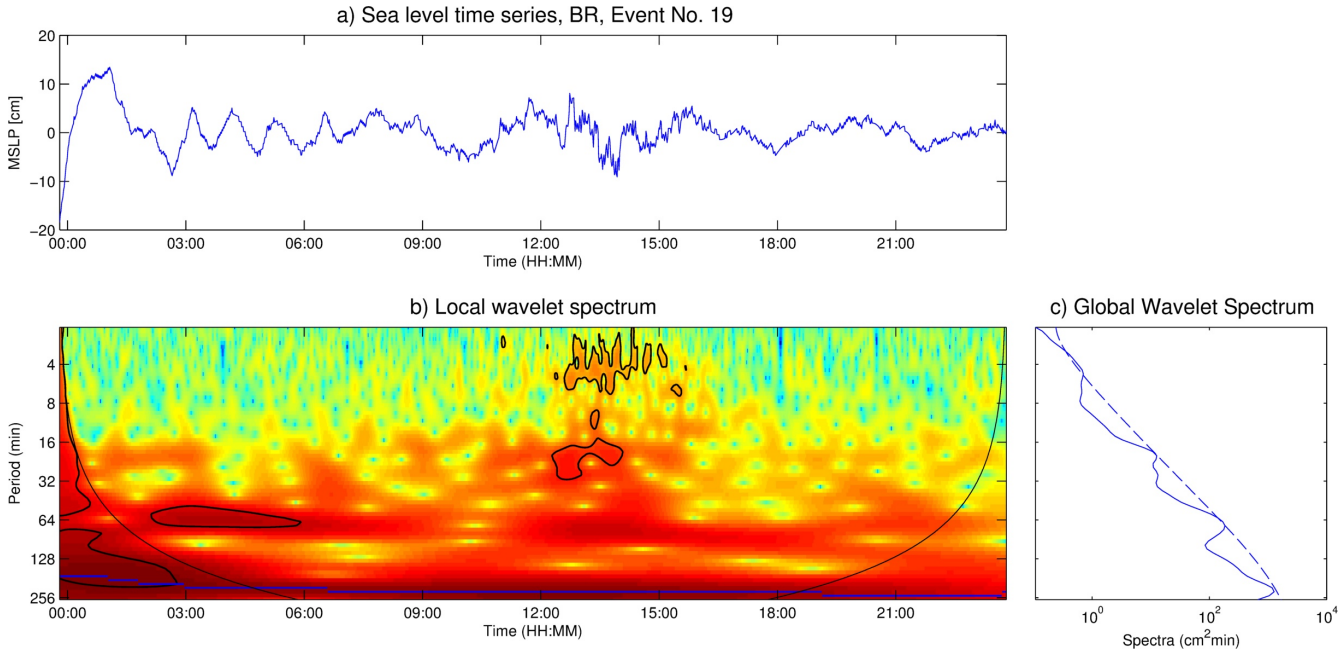

Figure 44: Sea level time series after 4-h high-pass filtering and its wavelet power spectra at BR.

Numerical simulation

We tested model simulation, using two different forcing pressure series, artificial signal (Experiments I) and observed air pressure time series (Experiment II) following Hibiya and Kajiura (1982) and Vilibić et al. (2008) respectively. We find that both methods work well. The former method is rather focused on anticipating peak sea level, while with the latter method we can simulate the changing sea level at a site. This hints us that we can monitor long ocean waves on a delayed near-real time basis with a model forced by observed sea level pressure at islands/coasts. To do so, we first need estimated direction and

speed of air flow, which can be obtained from model outputs and synoptic observations. For example, we can produce simulated long ocean wave field every hour or three hours. The former method may be used to make forecast of long ocean waves, based on very-short to short range atmospheric forecasts.
We also tested the model with forcing fields using 2-dimensional optimal interpolation of 1-min MSLP data from the coastal sites of South Korea, but it did not work because pressure gradients are smoothed out due to lack of spatial resolution. Instead, it seems that 1-dimensional interpolation of time series connecting sea level sites and then applying of the scheme by Vilibić et al. (2008) is a possible approach to simulate sea levels at sites at once. This may be needed because an atmospheric disturbance over the Yellow Sea brings tsunami-like sea level oscillations to a large extension of coastal area.
Another finding is that if host model does not resolve high frequency waves, the nested model is necessitated to underestimate sea level because the host model feeds underestimated wave heights to the nested model. Thus using rotated grids instead of unstructured grids would be a good solution to increase resolution with a limited computing source.
In addition, since the Yellow Sea meteotsunami is a sea-traversing phenomena, using only a local domain around the coast does not make sense.

F Conclusion

A typical synoptic setting for meteotsunamis over the Yellow Sea were identified based on a total number of 49 meteotsunami events in spring (Mar-May) between 2002 and 2013 documented by the KMA. In addition, mean properties of long ocean waves and atmospheric disturbances and their energy transfer during the events were sought through spectral analysis and numerical experiments.
A typical synoptic setting favouring meteotsunami over the Yellow Sea is characterised by an jet stream shear over the Yellow Sea, which is related with generation of gravity waves. The jet stream shear forms a lingering relative vorticity max over Manchuria, which generates surface lows consecutively over the sea. The high frequency of occurrence of meteotsunami over the Yellow Sea in spring is attributed to this typical synoptic setting. The common features during significant atmospheric disturbances, observed at other places in the world, such as temperature inversion at the level of about 850 hPa and 500 hPa, and lower jet streams at the level of about 500 hPa, also appear over the region.
The maturing of jet streak from the north-west is related with the two atmospheric disturbance movement patterns: approaching from the north-west and the south-west. At the early stage, when the upstream sector is stronger, is more associated with the NW pattern, while at the decaying stage, when the downstream sector is stronger, the SW pattern more likely occurs.
Mean properties of the Yellow Sea meteotsunamis in spring may be expressed as: a mean atmospheric disturbance with a pressure change of 3.2 hPa for 37 min generates tsunami-like sea level oscillations with a mean amplitude of 21.5 cm at the west coast of South Korea by an amplification factor of 6.3 due to the Proudman resonance (by a factor of 2.3), shelf effect (by a factor of 1.3) and harbour resonance (by a factor of 2.3). However there may exist considerable uncertainty on harbour resonance factor, which depends on the dominant frequencies of the incoming long ocean waves, local natural periods and topography among others.
A numerical simulation shows that the disastrous event on 31 March 2007 at the west coast is due to high-frequency waves (periods of 2-8 min) with heights of 20-30 m reaching the entrance of harbours/bays/inlets. The incoming long ocean waves were further heightened up to about 130 cm due to harbour resonance. The energy source of those record-high waves is a box-type pressure disturbance, which is characterised by a high energy transfer efficiency from the disturbance to long ocean waves.
The Yellow Sea meteotsunami is a synoptic or mesoscale phenomenon in terms of propagating long ocean waves and travelling atmospheric disturbance, however high-frequency waves embedded in the

disturbance and seiches at coasts are characteristics of small scale phenomena. Therefore high-resolution grids covering the entire sea is required for forecasting meteotunami over the Yellow Sea. Furthermore at coastal areas much higher resolution models should be necessary. In this study we conducted numerical experiments with a very limited computing source, so we used rotated grids varying according to direction of atmospheric disturbance to increase resolution along the path of the disturbance, which was very successful.

The Yellow Sea meteotsunamis are characterised by a high frequency of occurrence in spring, more than 2/3 if February is included. The results of this study suggest possibilities of providing general short-term (2-3 days) meteotsunami forecast based on synoptic analysis in spring (Feb-May). In addition, in parallel with developing high-resolution atmospheric-oceanic coupled model, we propose developing model output statistics for meteotsunami forecasting as South Korea has a number of samples of events and a rich of temporal, spatial high-resolution observations of sea level and MSLP. To do so, research on natural periods along the west coastline and their sensitivities to atmospheric disturbances seems to be utmost important.

Appendix

Model Outputs

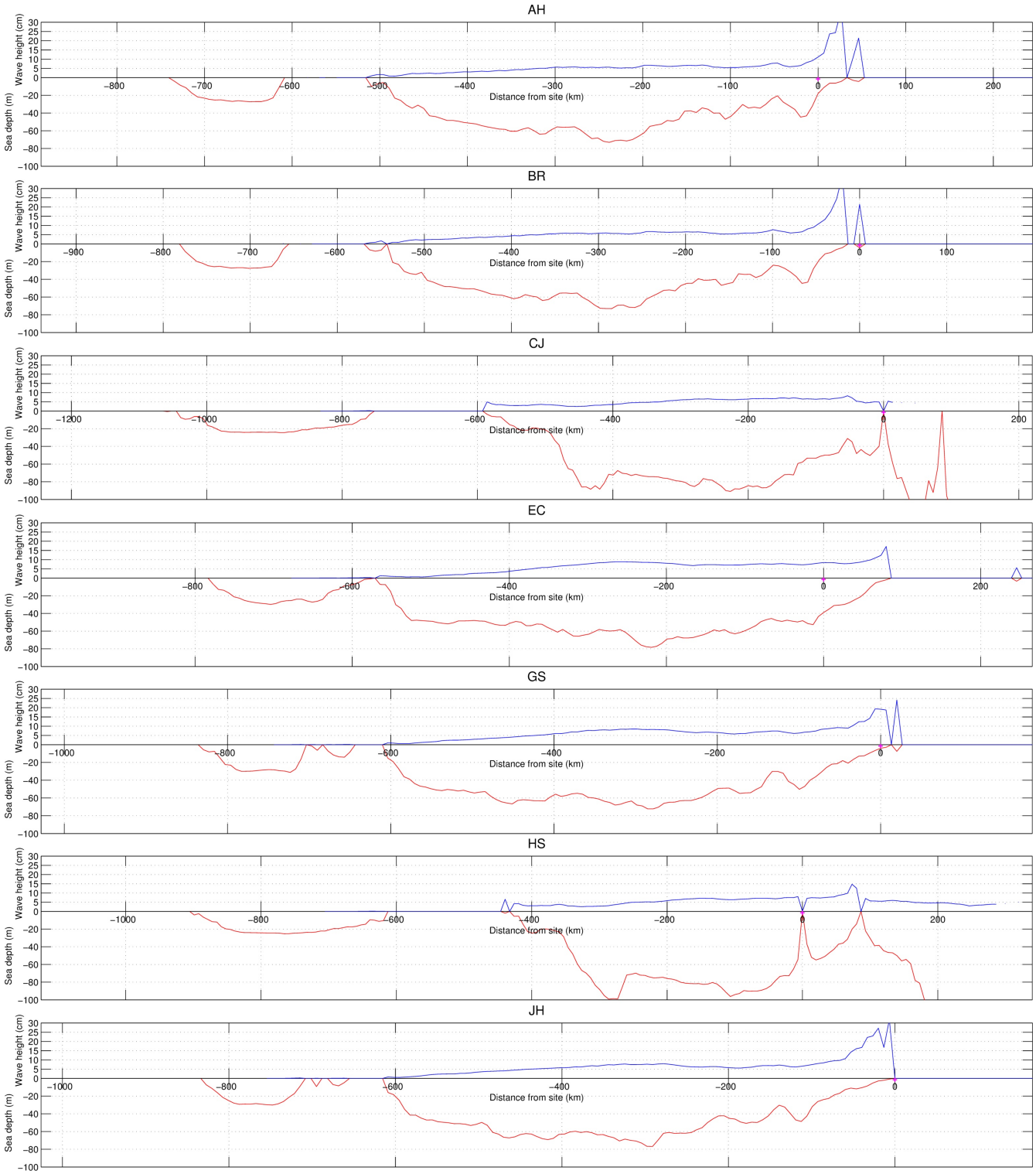

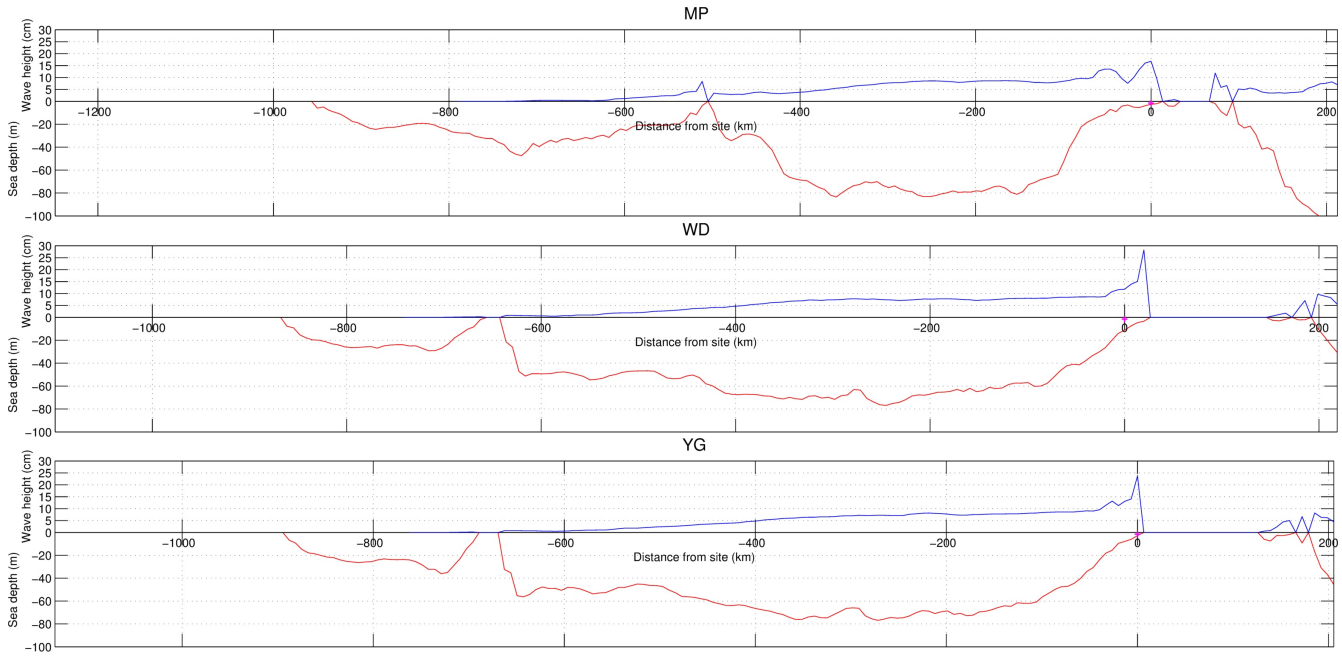
MP
Wave height (cm)
Sea depth (m)
Distance from site (km)
WD
Wave height (cm)
Sea depth (m)
Distance from site (km)
YG
Wave height (cm)
Sea depth (m)
Distance from site (km)

Acknowledgements

I owe my deepest gratitude to my supervisor Prof. Knut Barthel, Geophysical Institute, for the invaluable advice and support on this study in particular for modelling. Also, I would like to thank Chief Forecaster Dr. G.-I. Jang and Mr. H.-M. Eom at the Korea Meteorological Administration (KMA) for their inputs and advice on synoptic and spectral analysis. The sea level data from the 22 sites were provided by the Korea Hydrographic and Oceanographic Administration (KHOA), and the air pressure data from hundreds of sites were given by the Korea Meteorological Administration (KMA). I also would like to thank Ms. G.-N. Han and Mr. J.-H. Yun for that. The ERA-Interim reanalysis data were obtained from the ECMWF website: *apps.ecmwf.int/datasets/data/interim−full−daily/*. The sea depth data were retrieved from the GEBCO website: *www.gebco.net/data_and_products/gridded_bathymetry_data/*. The maps for some small areas were taken from Google Maps: *maps.google.com*.

References

Bjornsson, H. and Venegas, S. A. (1997). A manual for EOF and SVD analyses of climatic data. Technical report, Department of Atmospheric and Oceanic Sciences and Centre for Climate and Global Change Research, McGill University.

Cho, K.-H., Choi, J.-Y., Park, K.-S., Hyun, S.-K., Oh, Y., and Park, J.-Y. (2013). A synoptic study on tsunami-like sea level oscillations along the west coast of Korea using an unstructured-grid ocean model. *Journal of Coastal Research*, Special Issue No. 65.

Emery, W. J. and Thomson, R. E. (2004). *Data Analysis Methods in Physical Oceanography*, chapter 5.10.8, pages 540–545. Elsevier, second and revised edition.

Eom, H.-M., Seung, Y. H., Woo, S.-B., and You, S. H. (2012). Analysis of abnormal wave at the west coast on 31 march 2007 (in Korean). *International Journal of Ocean Engineering and Technology*, pages 217–227.

Hibiya, T. and Kajiura, K. (1982). Origin of the abiki phenomenon (a kind of seiche) in Nagasaki Bay. *Journal of the Oceanographical Society of Japan*, pages 172–182.

Jansa, A., Monserrat, S., and Gomis, D. (2007). The rissaga of 15 june 2006 in Ciutadella (Menorca), a meteorological tsunami. *Advances in Geosciences*, 12, 1–4,.

Jones, R. G., Murphy, J. M., and Noguer, N. (1995). Simulation of climate change over europe using a nested regional-climate model: I: Assessment of control climate, including sensitivity to location of lateral boundaries. *Quart. J. Roy. Meteor. soc.*, 526:1413–1449.

Kalnay, E. (2003). *Atmospheric Modelling, Data Assimilation and Predictability*, chapter 3.5, pages 123–124. Cambridge University Press.

KMA (2013). Investigation on the physical mechanism of abnormal waves in Korea and forecasting system construction plan (in Korean). Technical report, KMA.

Monserrat, S. (1996). Use of ducting theory in an observed case of gravity waves. *Journal of the Atmospheric Sciences*, 53:1724–1736.

Monserrat, S., Ibbetson, A., , and Thorpe, A. J. (1991). Atmospheric gravity waves and the 'rissaga' phenomenon. *Q. J. R. Meteorol. Soc.*, 117:553–570.

Monserrat, S. and Thorpe, A. (1992). Gravity-wave observations using an array of microbarographs in the Balearic Islands. *Q.J.R. Meteorol. Soc.*, 38:259–281.

Monserrat, S., Vilibić, I., and Rabinovich, A. B. (2006). Meteotsunamis: Atmospherically induced destructive ocean waves in the tsunami fre- quency band. *Nat. Hazards Earth Syst. Sci.*, pages 1035–1051.

Orlanski, I. (1984). A simple boudary condition for unbounded hyperbolic flows. *J. Comp. Sci.*, 21(3):251–269.

Pavelin, E. and Whiteway, J. A. (2002). Gravity wave interactions around the jet stream. *Geophysical Research Letters*, 29.

Proudman, J. (1929). The effects on the sea of changes in atmospheric pressure. *Geophysical Journal International*, page 197–209.

Rabinovich, A. and Monserrat, S. (1996). Meteorological tsunamis near the Balearic and Kuril Islands: Descriptive and statistical analysis. *Natural Hazards*, 13:55–90.

Rabinovich, A. B. (2009). *Handbook of Coastal and Ocean Engineering*, page 193–236. World Scientific Publ., Singapore.

Raymond, W. H. and Kuo, H. (1984). A radiation boundary condition for multi-dimensional flows. *Quart. J. R. Met. Soc.*, 110:535–551.

Thomson, R., Rabinovich, A., Fine, I., Sinnott, D., McCarthy, A., Sutherland, N., and Neil, L. (2009). Meteorological tsunamis on the coasts of British Columbia and Washington. *Physics and Chemistry of the Earth*.

Torrence, C. and Compo, G. P. (1998). A practical guide to wavelet analysis. *Bulletin of the American Meteorological Society*, pages 61–78.

Vilibić, I. (2005). Numerical study of the Middle Adriatic coastal waters' sensitivity to the various air pressure travelling disturbances. *Annales Geophysicae*, 23:3569–3578.

Vilibić, I., Monserrat, S., Rabinovich, A., and Mihanović, H. (2008). Numerical modelling of the destructive meteotsunami of 15 june, 2006 on the coast of the Balearic Islands. *Pure and Applied Geophysics*, 165.

Vilibić, I. and Šepic, J. (2009). Destructive meteotsunamis along the eastern Adriatic coast: Overview. *Physics and Chemistry of the Earth*, 34:904–917.

Šepić, J., Vilibić, I., and Belušić, D. (2009). Source of the 2007 1st meteotsunami (Adriatic Sea). *Journal of Geophysical Research*, 114(C03016).

Šepić, J., Vilibić, I., and Mahović, N. (2012). Northern Adriatic meteorological tsunamis: Observations, link to the atmosphere, and predictability. *Journal of Geophysical Research*, 117.